Paleoceanography and Paleoclimatology

RESEARCH ARTICLE
10.1029/2021PA004287

Key Points:

- Oceanic Anoxic Event 2 was characterized by multiple carbon cycle perturbations before and during the event
- The carbon isotopic composition of marine CO_2, and pCO_2 is estimated using carbon isotopes in carbonate and marine biomarkers
- The carbon isotopic composition of atmospheric CO_2 is estimated using the carbon isotopic composition of terrestrial biomarkers

Supporting Information:

Supporting Information may be found in the online version of this article.

Correspondence to:

F. G. Boudinot,
garrett.boudinot@cornell.edu

Citation:

Boudinot, F. G., Kopf, S., Dildar, N., & Sepúlveda, J. (2021). Carbon cycling during Oceanic Anoxic Event 2: Compound-specific carbon isotope evidence from the Western Interior Seaway. *Paleoceanography and Paleoclimatology*, *36*, e2021PA004287. https://doi.org/10.1029/2021PA004287

Received 28 APR 2021
Accepted 29 JUL 2021

Carbon Cycling During Oceanic Anoxic Event 2: Compound-Specific Carbon Isotope Evidence From the Western Interior Seaway

F. Garrett Boudinot[1,2,3], Sebastian Kopf[1,2], Nadia Dildar[1,2], and Julio Sepúlveda[1,2]

[1]Department of Geological Sciences, University of Colorado Boulder, Boulder, CO, USA, [2]University of Colorado Boulder, Institute of Arctic and Alpine Research, Boulder, CO, USA, [3]Now at Department of Ecology and Evolutionary Biology, Cornell University, Ithaca, NY, USA

Abstract The Cenomanian-Turonian Oceanic Anoxic Event 2 (OAE2, ~94 Ma) was a period of widespread ocean deoxygenation and marine organic carbon burial. Increased CO_2 and nutrient flux before OAE2 are generally considered the main drivers of ocean anoxia and carbon burial, though some evidence has suggested multiple phases of CO_2 input and burial throughout the event. To test hypotheses about the nature of carbon cycle perturbations before and during OAE2, we analyzed stable carbon isotopes in marine-derived and terrestrial-derived biomarkers from an expanded sedimentary record of OAE2 from the western margin of the Western Interior Seaway. Biomarker carbon isotope data were used to estimate the concentration and carbon isotopic composition of aqueous and atmospheric CO_2, as well as changes in marine productivity, through OAE2. While complicated by biological and environmental uncertainties, our pCO_2 reconstructions generally agree with estimates from other locations and proxies around the world. High-resolution sampling revealed several short-lived carbon cycle perturbations before and during OAE2 that may reflect fluctuations in the global carbon cycle, including several pulses of isotopically light carbon before OAE2, during the onset of OAE2, and during the Plenus event. This study provides new constraints on carbon cycle dynamics during OAE2 that highlight the complex nature of the event and its causes.

Plain Language Summary Oceanic Anoxic Event 2 (OAE2) was a period of dramatic climate change ~94 million years ago, characterized by high atmospheric CO_2, warm temperatures, and changes in ocean chemistry. While decades of research have identified the climate and ecological impacts of OAE2, there are still questions about how much, and how fast, the carbon cycle changed. We analyzed the carbon chemistry of biomolecules from plants, algae, and bacteria that lived during OAE2, and were preserved in ancient seafloor sediments found in modern-day Utah. We used our results to estimate important metrics for understanding the carbon cycle during the event, including the composition of carbon in the oceans and atmosphere, and the concentration of atmospheric CO_2. Our results show that there were multiple increases in atmospheric CO_2 throughout OAE2. This study paints a more refined picture of how the global carbon cycle was impacted during climate change in Earth's history, which can be used to strengthen our understanding of climate change today and in the future.

1. Introduction

Oceanic Anoxic Event 2 (OAE2; ~94 Ma) was an interval of global change characterized by elevated atmospheric CO_2 (Freeman & Hayes, 1992; Bice et al., 2006; Hong & Lee, 2012; Sinninghe Damsté et al., 2008; Witkowski et al., 2018), altered nutrient cycling (Monteiro et al., 2012; Mort et al., 2007; Owens et al., 2016), and expanded ocean anoxia (Boudinot et al., 2020; Kuypers et al., 2002; Monteiro et al., 2012; Owens et al., 2013, 2016; Pancost et al., 2004; Sarmiento et al., 1988; Schlanger & Jenkyns, 1976; Sepúlveda et al., 2009; Takashima et al., 2006) making it a useful case study to investigate the effects of global climate change on marine biogeochemistry. Previous studies have revealed that the rapid input of mantle-derived CO_2 and nutrients before OAE2 (Barclay et al., 2010; DuVivier et al., 2014; Jones et al., 2020; Turgeon & Creasser, 2008) resulted in enhanced marine productivity (Kuypers et al., 2002; Leckie et al., 2002; Monteiro et al., 2012; Mort et al., 2007; Sepúlveda et al., 2009), water column deoxygenation (Boudinot et al., 2020; Kuypers et al., 2002; Monteiro et al., 2012; Owens et al., 2013, 2016; Pancost et al., 2004; Sepúlveda

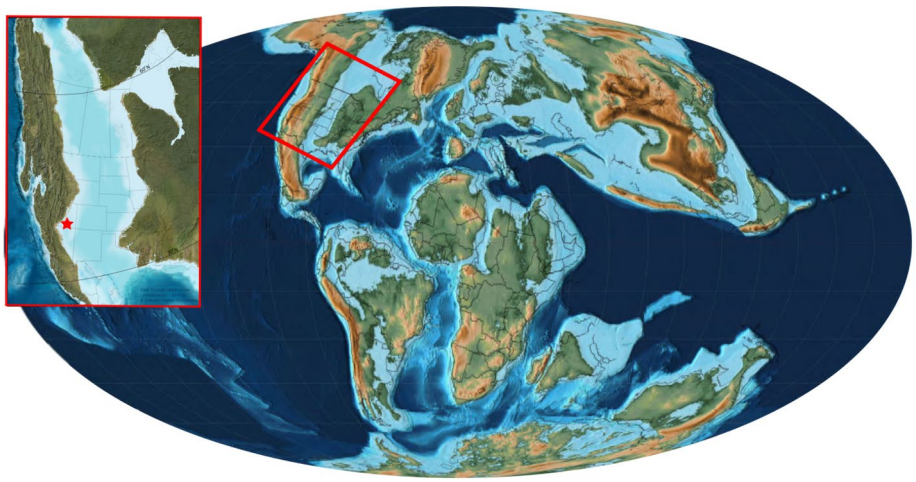

Figure 1. Paleomap of the Cenomanian (96.6 Ma; Scotese, 2014; © 2016 Colorado Plateau Geosystems Inc.). Red frame indicates the location of the inset map. Inset shows paleomap of the Western Interior Seaway over modern US states. Red star indicates the location of the SH#1 core (37.158466°N, 111.531947°W).

et al., 2009; Takashima et al., 2006), increased ocean temperature (Bice et al., 2006; Huber et al., 2002; O'Brien et al., 2017; Wilson & Norris, 2001), and ultimately widespread marine organic carbon burial during OAE2 (Arthur et al., 1987; Schlanger & Jenkyns, 1976). Questions remain, however, concerning the nature of the carbon cycle perturbations within the OAE2 event itself (e.g., Boudinot & Sepúlveda, 2020; O'Connor et al., 2019).

OAE2 sediments are identified and globally correlated by carbon isotope chemostratigraphic phases that reflect marine carbon burial and CO_2 inputs during the event (Erbacher et al., 2005; Hilbrecht & Hoefs, 1986; Jones et al., 2019; Sageman et al., 2006; Scholle & Arthur, 1980; Tsikos et al., 2004). The initial positive carbon isotope excursion (CIE), an interval of ^{13}C depletion known as the "Plenus" (Gale & Christensen, 1996; O'Connor et al., 2019), the remaining ^{13}C-enriched "plateau," and the return to ^{13}C-depleted values at the end of OAE2 each represent globally significant changes in the carbon isotopic composition of marine dissolved inorganic carbon (DIC; Schlanger et al., 1987). While such changes in the isotopic composition of atmospheric CO_2 likely occurred as well (e.g., Bohm et al., 1996; Gruber et al., 1999; Sheu et al., 1996), the impacts of OAE2 atmospheric CO_2 specifically remain poorly constrained, leaving questions about the relationship between atmospheric and oceanic carbon pools during OAE2.

Cell membrane lipids produced by marine and terrestrial autotrophs are preserved as biomarkers in black shales deposited during OAE2. Although biomarkers can be altered through diagenesis and catagenesis, they retain the carbon isotopic composition of the originally synthesized lipid, which is largely determined by isotopic fractionation during photosynthesis and the isotopic composition and concentration of the inorganic carbon substrate used (Hayes, 2001). As such, carbon isotope analyses of autotrophic biomarkers provide a means of investigating changes in the isotopic composition and concentration of carbon pools (i.e., dissolved marine aqueous CO_2 and atmospheric CO_2). For example, previous studies have measured changes in the carbon isotopic composition of some marine biomarkers from OAE2 as a means to estimate atmospheric CO_2 concentrations during the event (e.g., Bice et al., 2006; Freeman & Hayes, 1992; Sinninghe Damsté et al., 2008; van Bentum et al., 2012).

Records of the atmospheric partial pressure of CO_2 (pCO_2; e.g., Barclay et al., 2010; Bice et al., 2006; Sinninghe Damsté et al., 2008; van Bentum et al., 2012) and marine productivity (Boudinot et al., 2020; Bralower, 1988; Eicher & Diner, 1985; Elderbak & Leckie, 2016; Leckie, 1985; Leckie et al., 2002; Mort et al., 2007; Reolid et al., 2015; Sepúlveda et al., 2009) show considerable spatial and temporal variability through OAE2. Detailed questions concerning the timing and nature of biogeochemical feedbacks around OAE2, including the direct response of marine ecosystems to changes in pCO_2, the oceanographic controls on marine productivity, and the timing of CO_2 inputs at the onset of the event, require higher temporal resolution pCO_2 and productivity records. The Smokey Hollow #1 core (SH#1 core; Figure 1) presents an expanded sedimentary

record of OAE2 from the western margin of the Western Interior Seaway (WIS; Jones et al., 2019) that contains both marine-derived and terrestrially derived biomarkers (Boudinot & Sepúlveda, 2020; Boudinot et al., 2020), providing a high-resolution archive of marine and atmospheric carbon, respectively. Using carbon isotopes of biomarkers in the SH#1 core, we test the hypotheses that (a) carbon isotopes from marine-derived and terrestrial-derived biomarkers preserved in neritic ecosystems record changes in global and local carbon cycle dynamics, (b) that OAE2 was spurred by a pulse of CO_2 to the atmosphere before the event, (c) that the onset (initial CIE) of OAE2 was characterized by a unilateral drawdown of atmospheric and aqueous CO_2, and (d) that the Plenus event experienced multiple pulses of enhanced atmospheric CO_2 input.

We used the carbon isotopic composition of terrestrial plant waxes ($\delta^{13}C_{plant\text{-}wax}$; n-$C_{27,\ 29,\ 31,\ 33,\ 35}$; Eglinton & Hamilton, 1967) to trace the carbon isotopic composition of atmospheric CO_2 ($\delta^{13}C_{CO_2}$). We also used marine biomarker carbon isotopes ($\delta^{13}C_{marine\text{-}lipid}$) to assess lipid sources and trace changes in the carbon isotopic composition of dissolved CO_2 in the ocean ($\delta^{13}C_{CO_2\ -aq}$). Finally, we used carbon isotopes from phytane to estimate aqueous and atmospheric CO_2 concentrations at high temporal resolution through the event. To disentangle local changes (e.g., oceanography and productivity) from global carbon cycle perturbations, we compared the carbon isotope composition of marine biomarkers with terrestrial biomarkers in the SH#1 core, and compared those to previously reported records from other locations around the world. The resulting records of carbon cycle changes show several phases of CO_2 input before and during OAE2 and provide valuable information about the nature of the carbon cycle during an interval of global change in Earth history.

2. Materials and Methods

2.1. Study Area

The ~30-m long SH#1 core contains a continuous sedimentary record of the Tropic shale from the western margin of the WIS that captures the entire OAE2 event (Boudinot et al., 2020; Jones et al., 2019). Previous work has characterized the SH#1 core location as a neritic ecosystem setting (Boudinot et al., 2020; Jones et al., 2019) influenced by foredeep subsidence (Jones et al., 2019; Kauffman, 1984) and several cycles of sea-level rise and fall throughout OAE2 (Boudinot et al., 2020; Jones et al., 2019), with water depths between 50 and 100 m during the early Turonian highstand (Sageman & Arthur, 1994). We obtained 1-cm-thick core samples (integrating ~300 years based on the ~3 cm/kyr sedimentation rates calculated in Jones et al., 2019) at every 10 cm through the onset and early phases of OAE2 (representing ~3 kyr intervals; Jones et al., 2019), and every meter throughout the core (representing ~30 kyr intervals; Jones et al., 2019), with a total of 40 samples analyzed for compound-specific carbon isotopes. Bentonite layers, biostratigraphic indicators, astrochronology, and carbon isotope chemostratigraphy have aided in the basin-wide and global correlation of the SH#1 core with other OAE2 sections (Jones et al., 2019). Existing records from the SH#1 core, including carbon isotopes from bulk carbonate ($\delta^{13}C_{carb}$) and organic matter (OM; $\delta^{13}C_{org}$), and the diversity and abundance of lipid biomarkers and foraminifera, provide extensive information on the ecological dynamics at the core location during OAE2 (Boudinot et al., 2020; Jones et al., 2019).

2.2. Bulk Organic Carbon Isotope Analyses

$\delta^{13}C_{carb}$ and $\delta^{13}C_{org}$ from the SH#1 core record the main phases of the OAE2 carbon isotope chemostratigraphy (Jones et al., 2019). $\delta^{13}C_{carb}$ and $\delta^{13}C_{org}$ through the SH#1 core were reported in Jones et al. (2019), though not from the same samples used for biomarker analyses. We measured $\delta^{13}C_{org}$ in the same samples analyzed for biomarkers, as well as other samples throughout the SH#1 core (Figure 2a) using the sample preparation steps outlined in Brodie et al. (2011). Three grams of each sample was placed into glass centrifuge tubes, mixed with 10 ml of 10% HCl, vortexed, and allowed to react for up to an hour. The samples were then centrifuged at 1,000 rpm for 3 min, and ~75% of the acid solution was removed. Milli-Q water was then added to each sample and vortexed. The samples were then centrifuged at 100 rpm for 5 min, and ~75% of the supernatant was removed. This process was repeated until the pH of the solution matched that of the Milli-Q water. The remaining water was removed, and the samples were dried in an incubation oven at ~26°C for ~3 days. The dried decalcified powders were ground again to homogenize,

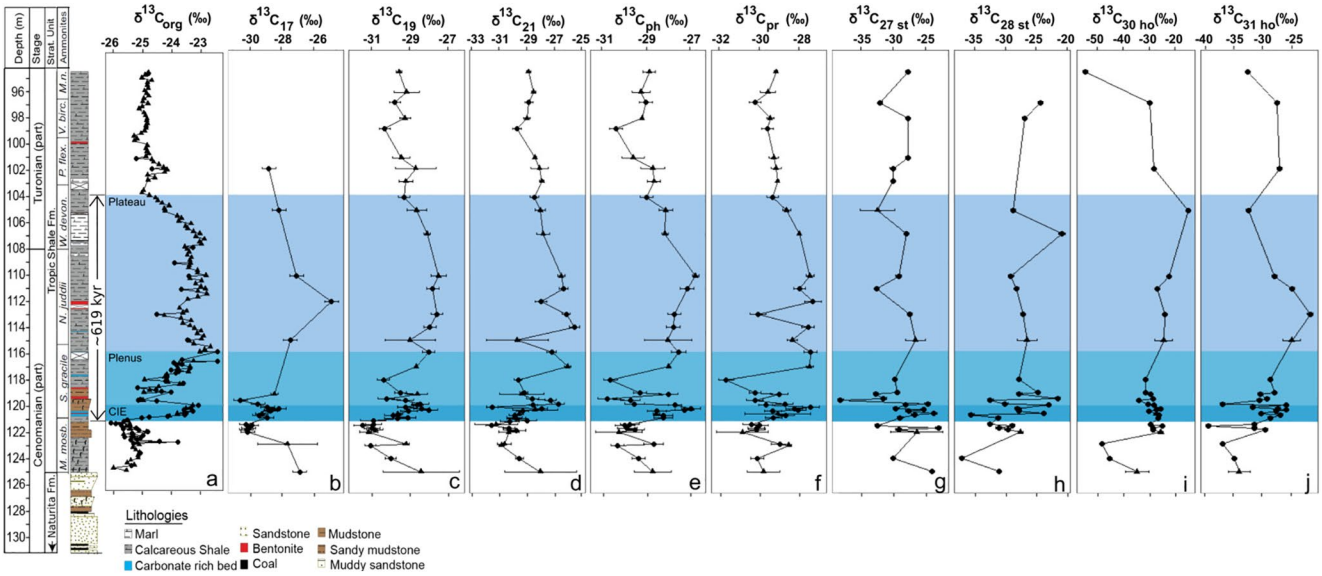

Figure 2. Carbon isotope record of bulk organic carbon and marine biomarkers show the main phases of the OAE2 chemostratigraphy. Lithology, ammonite zones, and timescale from Jones et al. (2019). (a) Bulk organic carbon isotopic composition ($\delta^{13}C_{org}$); triangles are data from Jones et al. (2019), circles are data from this study. (b) *n*-C_{17} (c) *n*-C_{19}, (d) *n*-C_{21}, (e) Phytane, (f) Pristane, (g) C_{27} $\alpha\alpha\alpha$ R cholestane, (h) C_{28} $\alpha\alpha\alpha$ R methylcholestane, (i) C_{30} $\alpha\beta$ hopane, and (j) C_{31}S hopane. For panels (b) through panel (j), circles are single-analysis predicted $\delta^{13}C$ values (based on the $\delta^{13}C$ calibration used) with their predicted standard error plotted, and triangles are duplicate analysis mean values with their standard deviation of duplicate analyses plotted. Variable *X*-axis values in each panel display the full range of $\delta^{13}C$ for each biomarker. Blue shading indicates the major phases of the OAE2 carbon isotope chemostratigraphy: the darkest blue indicates the initial carbon isotope excursion (CIE; 121.196–120 mcd), the medium blue indicates the Plenus interval (120–115.88 mcd), and the lightest blue indicates the plateau phase (115.88–103.93 mcd).

and then analyzed on a Thermo Scientific Delta V plus elemental analyzer-isotope ratio mass spectrometer in the University of Colorado Boulder Environmental Sciences Stable Isotope Lab. Acetanilide #1 (Arndt Schimmelmann, Indiana University; $\delta^{13}C = -29.53‰$) was used as a discrimination standard, L. glutamine (USGS 40; $\delta^{13}C = -14.71‰$) was used as a linearity and drift standard, and a low organic soil standard (EA Consumables; $\delta^{13}C = -27.34‰$) was used as a monitoring standard. Each sample was analyzed at least two times; reported values and error bars are the mean and standard deviations of those duplicate or triplicate analyses. Seventeen samples used for biomarker analyses were not analyzed for $\delta^{13}C_{org}$.

2.3. Compound-Specific Carbon Isotope Analyses

Biomarkers were extracted and purified as described in Boudinot et al. (2020). In brief, cleaned and powdered rock samples were extracted using a Dionex Accelerated Solvent Extractor (ASE) 200 with a mixture of dichloromethylene and methanol (DCM:MeOH 9:1 v:v). Inorganic sulfur was removed using acid-washed copper shots, and asphaltenes were removed by precipitation in hexane, freezing for at least 3 h, and subsequent centrifugation. The aliphatic fraction used in this study was eluted from maltenes using silica gel packed Pasteur pipette column chromatography with hexane (3/8 dead volume).

Urea adduction was used to isolate *n*-alkanes from branched and cyclic compounds in the aliphatic hydrocarbon fraction for samples through the pre-OAE2, CIE, and early Plenus phases. An aliquot of the aliphatic hydrocarbon fraction was evaporated in centrifuge tubes overnight and resuspended in 1.5 mL of a 2:1 hexane: acetone (v:v) solution. Then, 1 mL of a super-saturated urea solution was added, and samples were evaporated under a gentle N_2 flow until no solvent remained. 1 mL of DCM was added to the dried sample with urea crystals, followed by gentle vortexing and 10 min of centrifugation at 1,000 rpm before decanting the non-adducted phase with ~75% of the DCM. This process was repeated for a total of 4 rinses. Finally, 6 mL of Milli-Q water was added to each sample, followed by 2 mL of DCM. Samples were left to separate for 30 min before the adducted phase with *n*-alkanes was decanted with ~75% of the DCM. This process was repeated for a total of 3 rinses.

We analyzed the carbon isotopic composition of *n*-alkanes and other biomarkers (e.g., pristane, phytane, steranes, and hopanes) in the adducted phase and the total aliphatic hydrocarbon fraction, respectively, via gas chromatography-combustion-isotope ratio mass spectrometry (GC-C-IRMS) using a Thermo Scientific GC (Trace 1310) with Isolink II connected to a MAT 253 Plus IRMS. Several GC methods were used depending on sample type and date of analysis. Total aliphatic hydrocarbon fractions from low temporal-resolution samples were analyzed two times, first on a DB-5 GC column and then on a DB-1 to improve chromatographic separation of steranes and hopanes. For the analyses performed on the DB-5 column, the GC program was as follows: oven was held at 60°C isothermal for 2 min, then ramped to 150°C at 15°C/min, followed by a final ramp to 315°C at 4°C/min, held isothermal at 315°C for 10 min. The injection port was set on splitless mode, held at 250°C, with a split flow of 10 ml/min for 1 min and a purge flow of 5 ml/min. Aliphatic hydrocarbons and adducted aliquots separated on a DB-1 column used the same GC program as above. For those analyses, the instrument was equipped with a Programmable Temperature Vaporizing inlet with the following settings: 65°C–400°C at 8°C/s, held for 3 min, then on cleaning mode at 530°C for 5 min. Split flow was 50 ml/min, purge flow was 5 ml/min, and split-less time was 3 min. Helium carrier gas flow was held constant at 1.2 ml/min for all analyses. The A7 *n*-alkane standard mix (Arndt Schimmelmann, Indiana University, *n*-$C_{16\text{-}30}$; $\delta^{13}C$ range from −26.15‰ to −40.91‰) was used for linearity correction and isotopic calibration. All isotope calculations, data processing, and visualizations were performed in R (R Core Team, 2017), using the open-source carbon isotope data processing package Isoprocessor (https://github.com/isoverse/isoprocessor), and are available online (https://doi.org/10.1594/PANGAEA.933277). All isotopic data are reported in permil (‰) on the VPDB scale.

2.4. Estimating $\delta^{13}C_{CO_2\text{-}aq}$ Using $\delta^{13}C_{carb}$

We estimated $\delta^{13}C_{CO_2-aq}$ from $\delta^{13}C_{carb}$ as described elsewhere (Bice et al., 2006; Romanek et al., 1992; Sinninghe Damsté et al., 2008) using the following equation:

$$\delta^{13}C_{CO_2-aq} = \delta^{13}C_{carb} - 1 + \varepsilon_b, \quad (1)$$

where pH is assumed to have been constant, and ε_b is the temperature-dependent fractionation of CO_2 with respect to bicarbonate (Mook et al., 1974):

$$\varepsilon_b\left(‰\right) = 24.12 - \left(\frac{9866}{T}\right). \quad (2)$$

For ε_b, there were no available temperature (T) reconstructions for OAE2 from the SH#1 core location, or WIS, specifically. Thus, we used a temperature reconstruction based on the $\delta^{18}O$ of planktonic foraminifera from a similar latitude to the SH#1 core location (ODP site 1050, Blake Nose; 32°C; O'Brien et al., 2017), which is consistent with the mean temperature estimate from global planktonic foraminifera $\delta^{18}O$-derived temperature estimates during OAE2 (O'Brien et al., 2017). We used an existing record of $\delta^{13}C_{carb}$ through the SH#1 core (Jones et al., 2019), using a three-point linear interpolation model to fit data from that record to the depths used in this study. The samples that showed evidence of diagenetic alteration of carbonate at the base of the core (Jones et al., 2019) were excluded from this study.

2.5. Estimating $\delta^{13}C_{CO_2\text{-}aq}$ Using Marine $\delta^{13}C_{marine\text{-}lipid}$

Constraints on carbon isotope fractionation associated with photosynthesis and lipid biosynthesis between inorganic carbon and biomass (ε_{cell}), and between cell and lipid (ε_{lipid}) were used to estimate $\delta^{13}C_{CO_2-aq}$ from the carbon isotopic composition of selected marine lipids (e.g., phytane, $C_{17,\ 19,\ 21}$ *n*-alkanes). For ε_{cell}, we used the range of fractionation factors observed in algal cells of 12‰–21‰ (Ohkouchi et al., 2015; Table S1). For phytane, ε_{lipid} estimates range from 4‰ (Schouten et al., 1998; Sinninghe Damsté et al., 2008) to 6.4‰ (Riebesell et al., 2002; Sakata et al., 1997), and ε_{lipid} for short-chain *n*-alkanes ranges from 4‰ (Schouten et al., 1998; Sinninghe Damsté et al., 2008) to 8.4‰ (Sakata et al., 1997; Table S1). Minimum and maximum fractionation factors were used to produce minimum, maximum, and mean $\delta^{13}C_{CO2\text{-}aq}$ estimates (Figure S1).

2.6. Estimating $\delta^{13}C_{CO_2}$ Using $\delta^{13}C_{plant\text{-}wax}$

We also estimated $\delta^{13}C_{CO_2}$ through the onset of OAE2 using $\delta^{13}C_{plant\text{-}wax}$ and existing information on carbon isotope fractionation between atmospheric CO_2 and leaf carbon (ε_{leaf}; Ehleringer & Cerling, 2001), and between leaf and lipid carbon ($\varepsilon_{plant\text{-}wax}$; Diefendorf et al., 2011), associated with photosynthesis and lipid biosynthesis (Table S1). Given the predominance of C_3 photosynthesis in plants in the Cretaceous (Osbourne & Beerling, 2006; Sage, 2004), and constraints from our $\delta^{13}C_{CO_2-aq}$ estimates (Supporting Information S1), we used the minimum C_3 ε_{leaf} value of 22‰ (Ehleringer & Cerling, 2001). We also used the minimum gymnosperm $\varepsilon_{plant\text{-}wax}$ by plant wax chain length (Diefendorf et al., 2011) given the predominance of gymnosperms in the mid-Cretaceous (Belcher & Hudspith, 2016). The full range of C_3 ε_{leaf} and gymnosperm $\varepsilon_{plant\text{-}wax}$ (i.e., including maximum values) were used to calculate the full range (i.e., uncertainty) of those estimates as well (Figure S2).

2.7. Estimates of Carbon Isotope Fractionation During Photosynthesis (ε_p) Using $\delta^{13}C_{marine\text{-}lipid}$

Changes in CO_2 concentrations and phytoplankton growth rates have been inferred from biomarker carbon isotopes based on the increased carbon isotope fractionation of marine photoautotrophic photosynthesis under higher extracellular carbon concentrations (Popp et al., 1989). This relationship (ε_p) is expressed by relating estimated primary photosynthate $\delta^{13}C$ ($\delta^{13}C_p$) with $\delta^{13}C_{CO_2-aq}$ using the equation:

$$\varepsilon_p = 10^3 \left[\frac{\delta^{13}C_{CO_2-aq} + 1000}{\left(\delta^{13}C_p + 1000\right) - 1} \right]. \quad (3)$$

We used the carbonate-derived $\delta^{13}C_{CO_2-aq}$ for Equation 3, which is consistent with previous applications of ε_p (e.g., Bice et al., 2006; Freeman & Hayes, 1992; Witkowski et al., 2018). $\delta^{13}C_p$ was calculated as:

$$\delta^{13}C_p = \delta^{13}C_{marine-lipid} + \varepsilon_{lipid}. \quad (4)$$

We only used $\delta^{13}C_{marine\text{-}lipid}$ from phytane to estimate $\delta^{13}C_p$, and ultimately ε_p, as phytane is well constrained to predominantly algal sources (Hayes et al., 1990; Pancost et al., 1998), and its biosynthetic pathway is well understood (Supporting Information S1). Thus, ε_{lipid} for phytane was used for Equation 4 (Section 2.6; Table S1).

2.8. Estimating pCO_2 Using ε_p

Because ε_p is influenced by the concentration of extracellular aqueous CO_2, it has been used as a proxy for changes in the concentration of aqueous CO_2, and ultimately, atmospheric pCO_2 (Freeman & Hayes, 1992; Pagani et al., 2002; Popp et al., 1989). ε_p values were converted to aqueous CO_2 concentrations assuming passive diffusion of CO_2 to the site of photosynthesis (e.g., Bice et al., 2006; Freeman & Hayes, 1992; Witkowski et al., 2018):

$$\varepsilon_p = \varepsilon_f - \left(\frac{b}{\left[CO_2(aq)\right]} \right), \quad (5)$$

where ε_f is the maximum isotopic fractionation associated with algal photosynthesis, 25‰ (Bridigare et al., 1997; Goericke & Fry, 1994; Pagani et al., 2002). We used *b*-values of 170–220 to represent normal to elevated productivity scenarios, respectively, which is consistent with previous applications of the ε_p pCO_2 proxy (Bice et al., 2006; Hollis et al., 2019; Sinninghe Damsté et al., 2008; van Bentum et al., 2012; Witkowski et al., 2018), and is supported by previous work showing eutrophic conditions through OAE2 at the SH#1 core location (Boudinot et al., 2020). Maximum and minimum CO_2 concentration estimates derive from that range of *b*-values (Equation 5).

Aqueous CO_2 was converted to atmospheric pCO_2 using Henry's Law and assuming equilibrium between aqueous and atmospheric CO_2 (see Section 4.4.1):

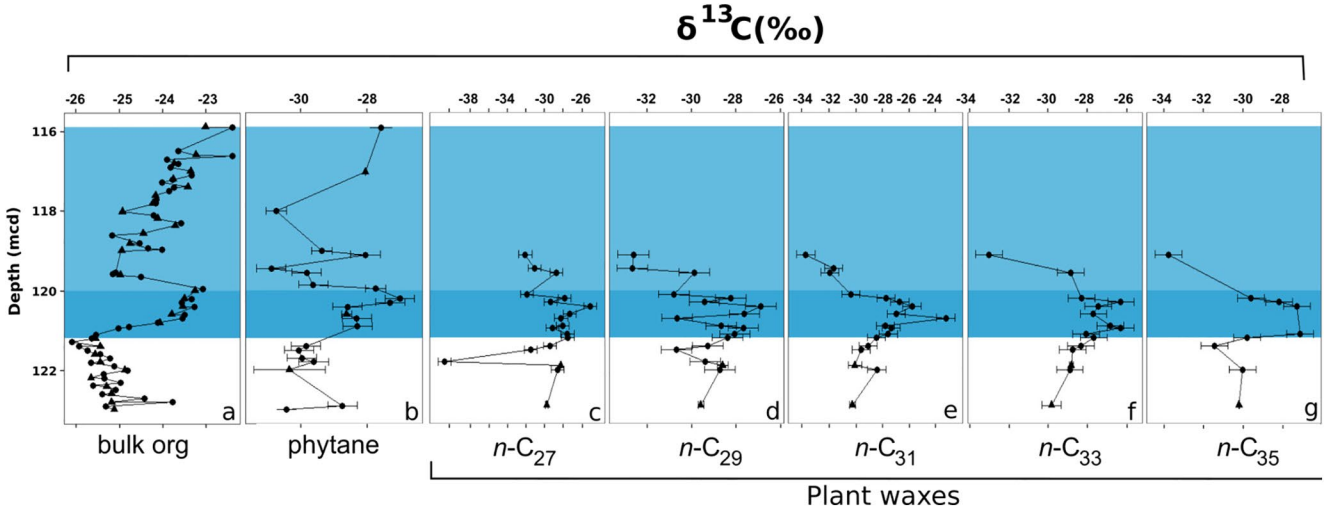

Figure 3. High-resolution carbon isotope records through the pre-OAE2 and early-OAE2 interval. (a) Bulk organic carbon ($\delta^{13}C_{org}$) as in Figures 2a and 2b phytane, (c) *n*-C_{27}, (d) *n*-C_{29}, (e) *n*-C_{31}, (f) *n*-C_{33}, and (g) *n*-C_{35}. Symbol type and error bars for panels (c)–(g) are the same as in Figure 2. Variable *X*-axis values in each panel display the full range of $\delta^{13}C$ for each biomarker. Blue shading is the same as in Figure 2, with the plateau phase not shown.

$$pCO_2 = \frac{\left[CO_2(aq)\right]}{K_0} \quad (6)$$

where K_0 is the solubility constant (Weiss, 1974). We used salinity estimates for the WIS (30 ppt salinity; Hay et al., 1996; Petersen et al., 2016) and the same temperature estimate as described above estimating for $\delta^{13}C_{CO_2-aq}$ from $\delta^{13}C_{carb}$ (Section 2.4; Equation 2; 32°C) for our K_0 value. K_0 was kept constant throughout the section, and the effect of variable salinity and temperature on final pCO_2 estimates was assessed using a sensitivity test with a range of K_0 values.

3. Results

3.1. Compound-Specific Carbon Isotope Records

Short-chain ($C_{17, 19, 21}$) *n*-alkanes, pristane, and phytane $\delta^{13}C$ values generally range from −32‰ to −27‰ (Figure 2). $\delta^{13}C$ values from algal steranes (C_{27} *ααα* R cholestane, C_{28} *ααα* R methylcholestane, hereafter C_{27} and C_{28} steranes, respectively) range from −38‰ to −20‰, while bacterial hopane (C_{30} *αβ* and C_{31} S, hereafter C_{30} and C_{31} hopanes) $\delta^{13}C$ values range from −55‰ to −15‰ (Figure 2). All $\delta^{13}C_{marine\text{-}lipid}$ records (except steranes) show the major features of the OAE2 carbon isotope chemostratigraphy observed in the $\delta^{13}C_{org}$ record (Figure 2). Additionally, most marine and terrestrial biomarkers (*n*-$C_{17, 19, 21}$, pristane, phytane, C_{27} sterane, C_{28} sterane, C_{31} S hopane, and *n*-$C_{27, 29, 31, 35}$) show a ^{13}C depletion (~2‰ for pristane, phytane, short-chain *n*-alkanes, and most plant waxes) before the CIE phase (~121.5 meters core depth, mcd; Figures 2 and 3), and marine and terrestrial biomarkers show a short-lived ^{13}C depletion (~1‰ for marine biomarkers, ~2‰–4‰ for plant waxes) during the CIE phase (120.6 mcd; Figures 2 and 3; except for C_{27} and C_{28} steranes). All biomarkers show a ^{13}C depletion (~3‰–4‰ for pristane, phytane, and short-chain *n*-alkanes, ~6‰–10‰ for plant waxes) at the start of the Plenus (~19.9 mcd; Figures 2 and 3). Some marine and terrestrial biomarkers (*n*-C_{19}, *n*-C_{21}, phytane, pristane, *n*-$C_{27,}$ *n*-C_{29}) show a short interval of ^{13}C enrichment (~1‰–3‰ for pristane, phytane, and short-chain *n*-alkanes) in the first half of the Plenus (119–119.5 mcd), and some (*n*-C_{19}, *n*-C_{21}, phytane, and pristane) show another ^{13}C depletion (~2‰–4‰) toward the middle of the Plenus (~118 mcd; Figure 2). Pristane, phytane, *n*-C_{19}, and *n*-C_{21} show a short interval of ^{13}C depletion in the early plateau (115 mcd; Figure 2). All marine biomarkers (except C_{27} sterane) show their most ^{13}C-enriched values in the plateau interval, and a ^{13}C depletion through the mid-plateau and post-OAE2 intervals (Figure 2; 110–99 mcd; except for C_{27} and C_{28} steranes).

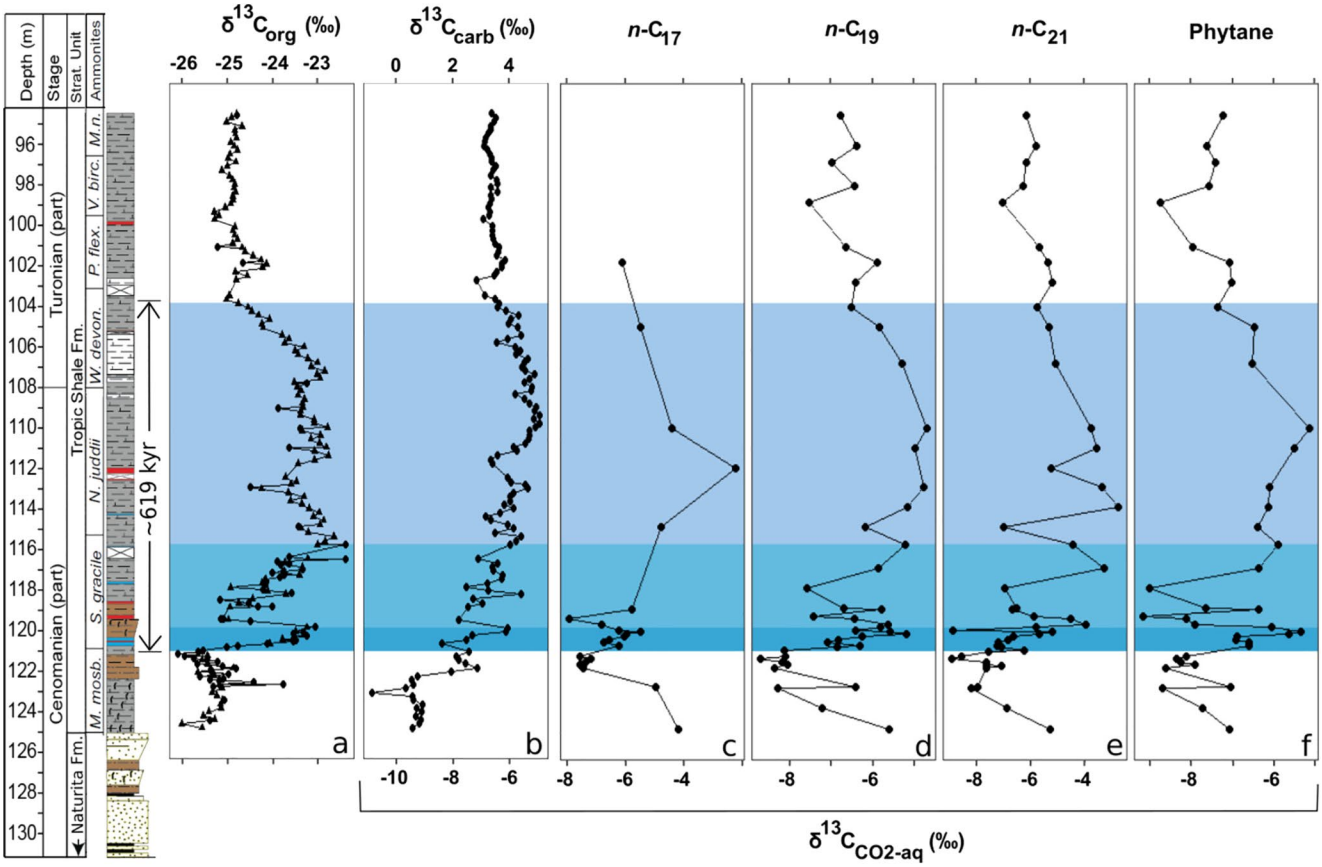

Figure 4. Carbonate-derived and biomarker-derived mean $\delta^{13}C_{CO_2-aq}$ values. (a) $\delta^{13}C_{org}$; (b) $\delta^{13}C_{CO2\text{-}aq}$ from $\delta^{13}C_{carb}$; (c)–(h) $\delta^{13}C_{CO_2-aq}$ derived from the $\delta^{13}C$ of n-C_{17}, n-C_{19}, n-C_{21}, and phytane, respectively. Blue shading is the same as in Figure 2.

Plant waxes, which were only analyzed through the pre-OAE2, CIE, and early Plenus phases, also show a ^{13}C depletion before OAE2, a positive CIE at the onset of OAE2, and a ^{13}C depletion into the Plenus (Figure 3). $\delta^{13}C_{plant\text{-}wax}$ values generally range from −34‰ to −24‰, with the most ^{13}C-depleted values during the Plenus (except for n-C_{27}, which is most ^{13}C-depleted before OAE2), and the most ^{13}C enriched values during the CIE phase (Figure 3). Most plant waxes ($C_{27, 29, 33}$) also show a short-lived ^{13}C depletion during the CIE phase (Figure 3).

3.2. Carbonate-Derived $\delta^{13}C_{CO_2\text{-}aq}$ Estimates

Carbonate-derived $\delta^{13}C_{CO_2-aq}$ estimates (Figure 4b) generally range from −9.5‰ to −5‰, with the most ^{13}C-depleted values before the onset of OAE2 (up to 122 mcd). Thereafter (above 122 mcd), values range from −8‰ to −5‰. Carbonate-derived $\delta^{13}C_{CO_2-aq}$ shows a ~2‰ positive excursion through the CIE phase, punctuated by a short-lived ^{13}C depletion (~2‰) in the middle of the CIE phase (~120.6 mcd). Carbonate-derived $\delta^{13}C_{CO2\text{-}aq}$ then shows a 2‰ negative CIE back to pre-OAE2 values during the Plenus, with values becoming more ^{13}C enriched through the Plenus to the middle plateau. Post-OAE2 $\delta^{13}C_{CO_2-aq}$ values are much less variable, at ~−7‰ (Figure 4b).

3.3. Biomarker-Derived $\delta^{13}C_{CO_2\text{-}aq}$ Estimates

Average $\delta^{13}C_{CO_2-aq}$ estimates from marine-derived biomarkers (e.g., phytane, short-chain n-alkanes; Figures 4c–4f) range from −9‰ to −2‰, with all compounds showing the most ^{13}C-depleted values before the initial CIE and during the Plenus, and the most ^{13}C-enriched values during the middle of the plateau phase.

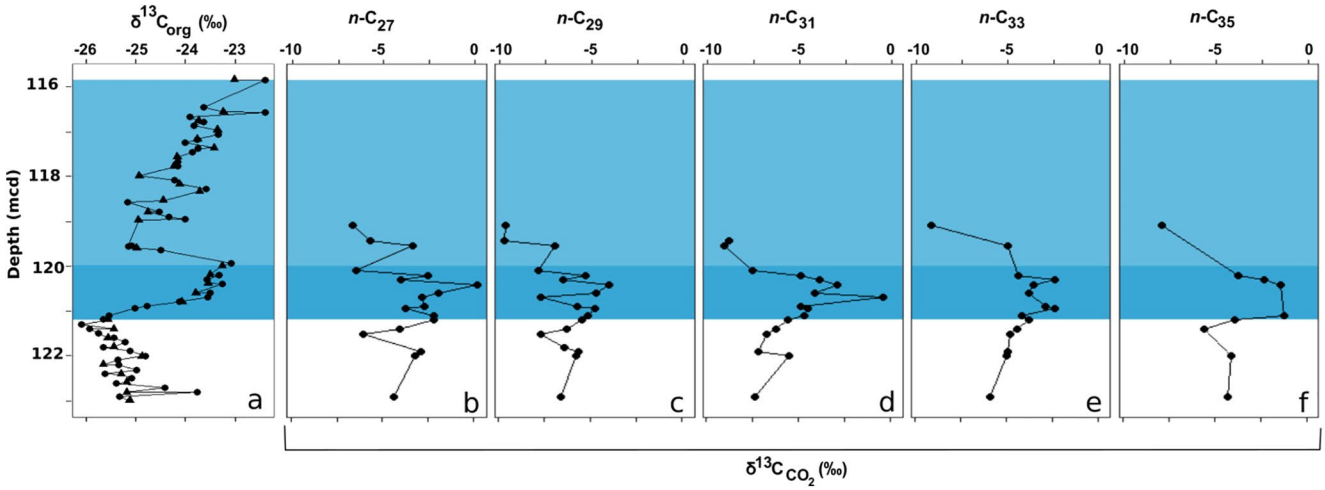

Figure 5. Atmospheric $\delta^{13}C_{CO2}$ estimates calculated using $\delta^{13}C_{plant\text{-}wax}$. (a) $\delta^{13}C_{org}$ as in Figures 2a and 2b n-C_{27}, with the lowest value at 121.8 mcd removed, (b) n-C_{29}, (d) n-C_{31}, (e) n-C_{33}, and (f) n-C_{35}. Shading is the same as in Figure 2.

All biomarker-derived average $\delta^{13}C_{CO_2\,-aq}$ estimates show the same features of the $\delta^{13}C_{marine\text{-}lipid}$ records (Figure 2), including ^{13}C depletion before the CIE, ^{13}C enrichment through the CIE punctuated by a short ^{13}C depletion, ^{13}C depletion in the Plenus punctuated by a short ^{13}C enrichment, ^{13}C enrichment at the end of the Plenus and through the early plateau, and ^{13}C depletion through the plateau and after OAE2. The full range of biomarker-derived $\delta^{13}C_{CO2\text{-}aq}$ estimates (i.e., minimum and maximum, rather than average) covered −15‰ to 5‰ (Figure S1).

3.4. Plant Wax-Derived $\delta^{13}C_{CO_2}$ Estimates

Plant wax-derived $\delta^{13}C_{CO_2}$ estimates (Figures 5b–5f) are generally between −10‰ and 0‰ throughout the pre-OAE2, CIE, and early Plenus phases. Several trends are evident in the record: a short ^{13}C-depletion before OAE2 (in all plant waxes but n-C_{33} at ~122 mcd), a slight ^{13}C-depletion during the otherwise ^{13}C enrichment trend through the CIE phase (for n-$C_{27,\ 29,\ 33}$ around 120.5 mcd), and a more pronounced negative CIE at the end of the CIE phase and into the Plenus phase (Figures 5b–5f). The full range of $\delta^{13}C_{CO_2}$ estimates from the spread of potential C_3 ε_{leaf} and gymnosperm plant wax-specific ε_{lipid} is from ~−10‰ to 15‰ (Figure S2).

3.5. Marine Biomarker-Derived Estimates of Carbon Isotope Fractionation During Photosynthesis (ε_p)

We calculated ε_p using the carbon isotopic composition of phytane (Figure 6b). ε_p values are lowest (14) at the base of the sampled section, and increase up to 18 by 122 mcd, just before the CIE (Figure 6b). ε_p decreases during the CIE, followed by an increase at the beginning (119.5 mcd) and middle (118 mcd) of the Plenus, and then a slight increase from the early plateau through the early Turonian (~100 mcd; Figure 6b).

3.6. Estimates of Aqueous CO_2 Concentrations and pCO_2

Estimates of both aqueous and atmospheric CO_2 concentrations (Figures 6c and 6d) show several pulses of increased CO_2, including an increase before OAE2 (~122 mcd), a decrease through the CIE (~120 mcd), two increases during the Plenus (119.5 and 118 mcd), rather stable levels during the Plateau, and a decrease and later increase just after OAE2 (~103–98 mcd). Aqueous CO_2 concentrations throughout the record ranged from ~15 to ~37 μmol/kg (Figure 6c). The conversion to pCO_2 was linear (Equation 6), and thus the pCO_2 record displays the same trends as the aqueous CO_2 record. pCO_2 estimates range from ~600 to ~1500 ppmv (Figure 6d).

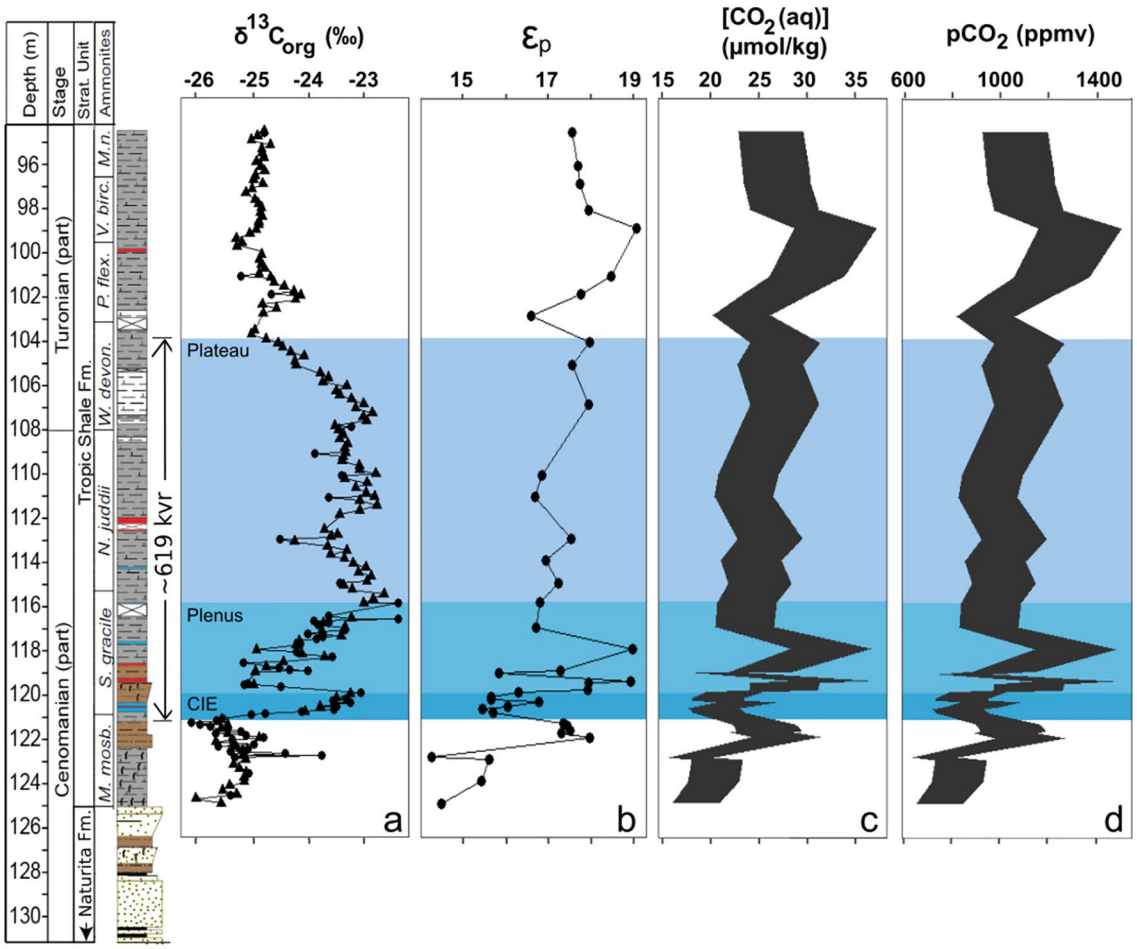

Figure 6. Estimates of aqueous CO_2 concentrations ([CO_2 (aq)]) and atmospheric pCO_2 from phytane-derived ε_p. (a) Bulk organic carbon isotopic composition as in Figures 2a and 2b changes in carbon isotopic fractionation (ε_p) associated with photosynthesis as derived from $\delta^{13}C_{phytane}$, (c) Aqueous CO_2 concentration estimates, and (d) Atmospheric pCO_2 estimates. Shading is the same as Figure 2.

4. Discussion

4.1. Compound-Specific Differences in the Magnitude of the Initial CIE

All biomarkers show the pronounced positive CIE at the onset of OAE2 (Table 1; Figures 2 and 3), though the magnitude of that CIE differs between biomarkers (Table 1; Supporting Information S1). Pristane and phytane show a CIE magnitude that is, consistent with that of bulk OM and carbonate, while other biomarkers such as steranes and hopanes show a much larger CIE magnitude (Table 1), likely due to changes in source organisms (i.e., input of soil bacteria below 122 mcd; Boudinot et al., 2020) and biosynthetic pathways (e.g., steranes; Supporting Information S1).

The magnitude of the initial CIE for pristane and phytane in the SH#1 core (3‰) is similar to that of phytane from other neritic ecosystems during OAE2 (~3‰–4‰), such as other WIS sections (Bunker Hill formation, Sinninghe Damsté et al., 2008; Greenhorn formation, Hayes et al., 1990) and in the Tethys (Tarfaya S13 core, Sinninghe Damsté et al., 2008; Livello Bonarelli, Pancost et al., 2004; Tsikos et al., 2004; Table 2), and is in line with the average CIE magnitude for bulk organic carbon and carbonate (~3‰) as well (Owens et al., 2018). Phytane from more distal locations like the equatorial Atlantic (ODP Site 367, Sinninghe Damsté et al., 2008), north Atlantic (ODP Site 603B, Sinninghe Damsté et al., 2008) and south Atlantic (ODP Site 530A, Sinninghe Damsté et al., 2008) show a larger CIE magnitude (~3.8‰–7‰) (Table 2). Such geographic variability of phytane-specific ^{13}C enrichment may indicate differences in the timing and degree of increased productivity between neritic and pelagic ecosystems during OAE2. Future work should

Table 1
Difference in the Magnitude of the Initial CIE at the Onset of OAE2 Between Different Biomarkers and Bulk Carbon

Class	Lipid biomarker	Pre-CIE (‰)	CIE max (‰)	Δ (‰)	Average δ (‰)
Plant waxes	*n*-C_{27}	−31.5	−25.3	6.2	4.18
	n-C_{29}	−30.7	−26.9	3.8	
	n-C_{31}	−30.2	−25.9	4.3	
	n-C_{33}	−28.8	−26.3	2.5	
	n-C_{35}	−31.5	−27.4	4.1	
Bacterial hopanes	C_{30} $\alpha\beta$	−29.7	−25.6	4.1	8.85
	$C_{31}S$	−39.3	−25.7	13.6	
Algal steranes	C_{27} $\alpha\alpha\alpha$ R	−32.5	−24.8	7.7	10.15
	C_{28} $\alpha\alpha\alpha$ R	−35.7	−23.1	12.6	
Aquatic *n*-alkanes	*n*-C_{17}	−30.3	−28	2.3	3.57
	n-C_{19}	−31.4	−27.9	3.5	
	n-C_{21}	−31.6	−26.7	4.9	
Phytol derivatives	Phytane	−30	−27	3	3
	Pristane	−30.4	−27.4	3	
Bulk organic carbon	–	−26	−23	3	3
Bulk carbonate	–	0.8	3.1	2.3	2.3

Note. Pre-CIE and carbon isotope excursion (CIE) max values were determined by the most ^{13}C depleted sample for each biomarker between 122 and 121.2 mcd (pre-CIE) and the most ^{13}C enriched sample between 121.1 and 120 mcd (CIE max).

investigate differences in the response of carbon burial and productivity to the drivers of OAE2 between neritic and pelagic ecosystems, which may have impacted the extent of ocean deoxygenation and the timescales of carbon burial.

4.2. Estimates of $\delta^{13}C_{CO_2\text{-}aq}$ From Biomarker and Carbonate $\delta^{13}C$

We used the carbon isotopic composition of marine biomarkers, in addition to existing information on the isotopic fractionation associated with their biosynthesis, to estimate the carbon isotopic composition of aqueous dissolved CO_2 (Section 2.6). While $\delta^{13}C_{carbonate}$ has been previously used to estimate the carbon isotopic composition of marine aqueous CO_2 (often described as DIC; e.g., Bice et al., 2006; Romanek et al., 1992; Sinninghe Damsté et al., 2008; van Bentum et al., 2012; Witkowski et al., 2018; though ε_b in Equation 1 accounts for aqueous CO_2 specifically), questions around the effects of pH, biology, and post-depositional alteration have limited confidence in those estimates (e.g., Hollis et al., 2019). In addition, some locations lack sufficient carbonate preservation for reliable site-specific carbonate-derived $\delta^{13}C_{CO_2-aq}$ estimates (e.g., Sinninghe Damsté et al., 2008). Thus, an alternative (e.g., biomarker-derived) $\delta^{13}C_{CO_2-aq}$ proxy could extend and improve studies of ancient carbon cycling.

We assessed the reliability of our $\delta^{13}C_{CO_2-aq}$ estimates derived from $\delta^{13}C_{marine\text{-}lipid}$ by comparing it with those derived from $\delta^{13}C_{carb}$ (Figure 4). The range of average $\delta^{13}C_{CO_2-aq}$ estimates from $\delta^{13}C_{marine\text{-}lipid}$ in the SH#1 core (−9‰ to −3‰ for all marine biomarkers and −9‰ to −5‰ for phytane; Figures 4c–4f), is similar to the $\delta^{13}C_{carb}$ -derived $\delta^{13}C_{CO_2-aq}$ estimates (−8‰ to −5‰; Figure 4b). Below 122 mcd in the SH#1 core, differences in $\delta^{13}C_{CO_2-aq}$ between those derived from carbonate and biomarkers (Figure 4) are likely due to diagenetic alteration of carbonates associated with changes in depositional environment (Jones et al., 2019), or due to varying $\delta^{13}C_{carb}$ values of different carbonate sources (e.g., Minoletti et al., 2005; Sepúlveda et al., 2019). That $\delta^{13}C_{CO_2-aq}$ estimates from both carbonate and biomarker carbon isotopes converge on −8‰ after 122 mcd (Figure 4) supports the interpretation that both carbonate and biomarkers accurately reflect surface water $\delta^{13}C_{CO_2-aq}$ above 122 mcd, and that the lower sea level below 122 mcd complicates the interpretation of $\delta^{13}C_{carb}$ records as has been shown elsewhere (Jones et al., 2019).

Both biomarker-derived and carbonate-derived $\delta^{13}C_{CO_2-aq}$ estimates integrate global and local signals. For example, aqueous CO_2 at the SH#1 core location may have been influenced by ^{13}C-depleted CO_2 from enhanced microbial respiration locally, as well as changes in the isotopic composition of carbon globally due to carbon burial elsewhere. $\delta^{13}C_{marine\text{-}lipid}$ is also sensitive to biological factors, such as changes in carbon isotope fractionation associated with cell geometry and growth rates (e.g., Bridigare et al., 1997; Pagani, 2014; Pancost et al., 1997), and changes in the relative proportion of dominant lipid sources through time (Supporting Information S1). On the other hand, as described above, $\delta^{13}C_{carb}$ in the SH#1 core was likely affected by sea-level changes and post-depositional alteration, particularly toward the base of the core (Boudinot et al., 2020; Jones et al., 2019). While the potential uncertainties associated with biosynthesis contribute to a wide range of uncertainty associated with biomarker-derived $\delta^{13}C_{CO_2-aq}$ estimates (Figure S1), again, the similarities between $\delta^{13}C_{CO_2-aq}$ estimate from carbonate and biomarkers indicate that average biomarker-derived $\delta^{13}C_{CO_2-aq}$ estimates (Figure 4) indeed reflect the $\delta^{13}C_{CO_2-aq}$ of the water column. Similarly, the reflection of the main phases of the globally correlated carbon isotope chemostratigraphy in both records supports the hypothesis that biomarkers and carbonate preserved in this marginal setting of the WIS indeed record changes in global carbon cycle dynamics.

Table 2
Magnitude of Phytane-Specific Carbon Isotope CIE (Δ) From Records in Other Locations Around the World During OAE2

Location	Biomarker	Δ (‰)
Site 367 (eastern Eq. Atlantic)	S-bound phytane	6
Site 1260 (western Eq. Atlantic)	S-bound phytane	7
Site 603B (western North Atlantic)	S-bound phytane	4.3
	Phytane	4.2
Site 530A (eastern South Atlantic)	Phytane	3.8
	S-bound phytane	5.2
Tarfaya S13 (eastern North Atlantic)*	S-bound phytane	4
	Phytane	3.1
Tarfaya S57 (eastern North Atlantic)*	S-bound phytane	4.3
Livello bonarelli (Tethys)*	Phytane	3.8
Greenhorn formation (eastern WIS)*	Phytane	3
	Pristane	3.1
Bunker Hill formation (central WIS)*	Phytane	4
SH#1 core (western WIS)*	Phytane	3
	Pristane	3

Note. Asterisk indicates sections from neritic environments/shallow water locations. The table presented in Sinninghe Damsté et al. (2008) with SH#1 core data added from this study.

Finally, we leveraged the carbonate-derived $\delta^{13}C_{CO_2-aq}$ values (~−8‰ to −5‰) to estimate the $\delta^{13}C$ of DIC at the SH#1 core location, using the information on the carbon isotope fractionation between aqueous CO_2 and total DIC (Deuser & Degens, 1976). The resulting SH#1 core location $\delta^{13}C_{DIC}$ estimates through OAE2 ranged from 0‰ to 3‰, which is strikingly similar to that of the modern ocean (~0‰–2‰; e.g., Humphreys et al., 2015). This additional $\delta^{13}C_{DIC}$ information from the SH#1 core location will be useful for future studies investigating global carbon cycling during OAE2 with comprehensive carbon isotope models.

4.3. Comparisons of $\delta^{13}C_{CO_2}$ and $\delta^{13}C_{CO_2\text{-}aq}$ Estimate

The general range of plant wax-derived $\delta^{13}C_{CO2}$ estimates from the SH#1 core at the onset of OAE2 (~−8‰ to −1‰; Figure 5) is similar to the average marine biomarker-derived $\delta^{13}C_{CO_2-aq}$ estimates (−9‰ to −3‰; Figure 4), as well as $\delta^{13}C_{CO_2}$ estimates through the Aptian (−10‰ to 0.5‰; Grocke, 2002). The general agreement between these estimates from different sources and methods support the use of $\delta^{13}C_{plant\text{-}wax}$ to estimate ancient $\delta^{13}C_{CO_2}$, and of $\delta^{13}C_{marine\text{-}lipid}$ to estimate $\delta^{13}C_{CO_2}$ (Figures 4 and 5; Supporting Information S1).

The ^{13}C depletion in atmospheric CO_2 before the CIE (~121.5 mcd; Figure 5) may derive from a previously identified pulse of volcanism before the CIE (Barclay et al., 2010; DuVivier et al., 2014; Jones et al., 2020; Turgeon & Creasser, 2008). Similarly, the ^{13}C depletion in $\delta^{13}C_{CO_2-aq}$ and $\delta^{13}C_{CO_2}$ in the middle of the CIE phase in the SH#1 core (~120.6 mcd; Figures 4 and 5) is also evident in a plant wax $\delta^{13}C$ record from near the coast of northwest Africa (Kuypers et al., 1999). The occurrence of this ^{13}C depletion during the CIE phase in $\delta^{13}C_{plant\text{-}wax}$ records from the Atlantic (Kuypers et al., 1999) and WIS (Figure 3), as well as in carbonate and marine lipids in the WIS (Figure 2), indicates a globally significant input of ^{13}C-depleted carbon to the ocean-atmosphere system during the otherwise positive CIE. Causes of the ^{13}C depletion are discussed below (Section 4.4). While local factors described above (e.g., changes in source organisms, post-depositional alteration) can influence $\delta^{13}C_{CO_2-aq}$ and $\delta^{13}C_{CO_2}$ proxies, the concomitant evidence of shorter-lived carbon cycle changes in aqueous and atmospheric CO_2 pools evidenced in our high-resolution record suggest that carbon cycle perturbations were more dynamic during OAE2 than previously recognized.

While marine biomarker-derived $\delta^{13}C_{CO_2-aq}$ and plant wax-derived $\delta^{13}C_{CO_2}$ estimates generally agree, differences in the timing and magnitude of the ^{13}C depletion during the Plenus between $\delta^{13}C_{CO_2}$ and $\delta^{13}C_{CO_2-aq}$ (Figures 4 and 5) indicate that the plant wax ^{13}C depletion during the late CIE and Plenus (after ~120.5 mcd) was likely influenced by local ecology, such as changes in plant ecosystem structure in the western US (Supporting Information S1). Further work is required to disentangle the effects of biological and global carbon cycle dynamics on the $\delta^{13}C_{plant\text{-}wax}$ record during the Plenus, as well as how other terrestrial carbon cycle dynamics influence the recording of $\delta^{13}C_{CO_2}$ in $\delta^{13}C_{plant\text{-}wax}$. Specifically, more work is required to investigate why plant wax-derived $\delta^{13}C_{CO2}$ corroborates $\delta^{13}C_{CO_2-aq}$ records before the mid-CIE (below ~120.5 mcd), but deviates in magnitude and timing of ^{13}C depletion thereafter (Figures 4 and 5).

4.4. Photosynthetic Carbon Isotopic Fractionation (ε_p) and pCO_2

4.4.1. Estimating pCO_2 From ε_p

The magnitude of carbon isotopic fractionation between lipids and the inorganic carbon substrate during photosynthesis, or ε_p (Freeman & Hayes, 1992; Popp et al., 1989; Sinninghe Damsté et al., 2008; Witkowski et al., 2018; Equation 3), has been used to infer changes in aqueous and atmospheric CO_2 concentrations

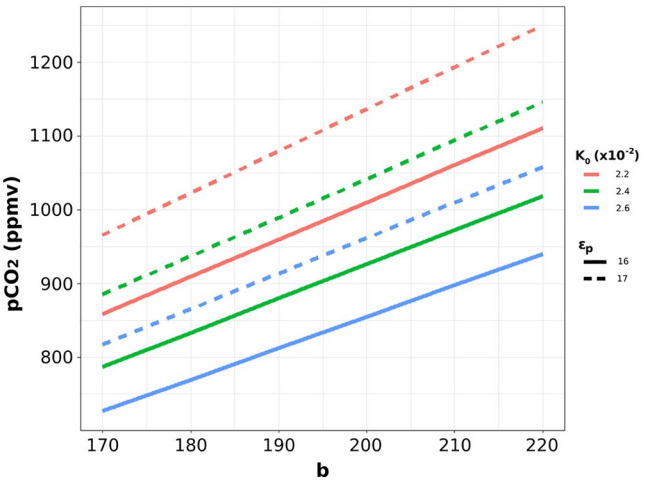

Figure 7. Sensitivity test showing the effect of *b*-values (*X*-axis; Equation 5), ε_p values (dashed and solid lines; Equation 5), and K_0 values (red, green, and blue colors; Equation 6) on final calculated pCO_2 (*Y*-axis; Section 2.9). These results indicate that *b*-values introduce the widest range of uncertainty (~200 ppmv), with non-CO_2 related ε_p changes (e.g., from growth rates) introducing uncertainty of ~100 ppmv, and salinity/temperature-dependent solubility constant (K_0) introducing uncertainty of ~150 ppmv.

(Freeman & Hayes, 1992; Popp et al., 1989), and phytoplankton growth rates (Pancost et al., 1997). Because evidence exists for changes in atmospheric CO_2 and marine productivity during OAE2 (e.g., Boudinot et al., 2020; Sinninghe Damsté et al., 2008; van Bentum et al., 2012), ε_p in the SH#1 core likely integrate both marine productivity and aqueous CO_2 concentrations. Specifically, ε_p increases can be driven by either increased aqueous CO_2 concentrations or decreased phytoplankton growth rates, while ε_p decreases can derive from either increased growth rates or decreased aqueous CO_2 concentrations (Popp et al., 1989).

We converted ε_p to aqueous CO_2 concentrations and atmospheric pCO_2 (Figure 6) assuming equilibrium between the water column and atmosphere, which at the neritic SH#1 core location can be complicated by a number of physical and biological factors. For example, dissolved CO_2 along the western margin of the WIS may not have been in equilibrium with the atmosphere due to elevated productivity (i.e., biological pump) and a shallow depth of OM remineralization in the water column (Boudinot et al., 2020). Sensitivity tests (Figure 7) show how uncertainties in *b*-values lead to larger pCO_2 uncertainties than salinity or temperature (reflected in solubility constants, K_0). This supports the use of *b*-values as an assessment of the overall uncertainties in pCO_2 estimates such as those shown in Figure 6. Similarly, given recent evidence that *b*-values may reflect environmental factors other than growth rate or nutrient availability (Hernández-Almeida et al., 2020), the wide range of *b*-values propagated throughout CO_2 calculations here reflects the uncertainties associated with many environmental and physiological factors driving the relationship between ε_p and CO_2.

Other potential uncertainties (Boudinot & Wilson, 2020) associated with local environmental and biological conditions, such as the strength of the biological pump, can be inferred to first order. For example, if aqueous CO_2 was out of equilibrium due to a strong biological pump—which is likely, given evidence of high productivity (Boudinot et al., 2020)—then our reported pCO_2 values may underestimate the actual pCO_2. On the other hand, evidence of intermittent shoaling of the chemocline during OAE2 at the SH#1 core location (Boudinot et al., 2020) may lead to overestimations of atmospheric pCO_2. Additionally, changes in nutrient and light availability may complicate the relationship between ε_p and CO_2 (Wilkes & Pearson, 2019). However, studies of ε_p in areas of the modern ocean have shown a stronger sensitivity of this pCO_2 proxy to atmospheric CO_2 in highly productive regions (Zhang et al., 2019), such as the SH#1 core location (Boudinot et al., 2020), supporting our use of ε_p for calculating ancient pCO_2. Furthermore, comparisons with pCO_2 records from other sections and proxies worldwide (described below) provide an independent assessment of the validity of pCO_2 values calculated here, and show that the pCO_2 range calculated from the SH#1 core is consistent with that from other proxies and locations.

While some scatter exists in the SH#1 core ε_p record and resulting pCO_2 estimates, several features are evident (Figure 6): (a) an increase in ε_p and pCO_2 before the initial CIE (up to 121 mcd), (b) a decrease in ε_p and pCO_2 during the initial CIE, (c) two increases in ε_p and pCO_2 during the Plenus interval (at ~119.5 and ~118 mcd), and (d) a gradual ε_p and pCO_2 increase through the plateau and post-OAE2 interval (from 112 up to 111 mcd).

4.4.2. pCO_2 From ε_p Before, During, and After OAE2

The increase in ε_p before 121 mcd coincides with biomarker trends that suggest an increase in productivity at the SH#1 core location (Boudinot et al., 2020), as well as evidence for increased volcanic CO_2 input globally (e.g., Barclay et al., 2010; Jones et al., 2020). Thus, the increased ε_p before OAE2 likely resulted from increased aqueous CO_2 concentrations (and pCO_2) from pre-OAE2 volcanism (Figure 6b). Oceanographic changes before OAE2 shown in other geochemical records (e.g., Ostrander et al., 2017; Owens et al., 2016) may have been related to such volcanism and CO_2 inputs.

The ε_p decrease after 122 mcd (during the onset of the initial CIE) may be best explained by an increase in phytoplankton growth rates. Boudinot et al. (2020) evidenced a strengthened chemocline at the SH#1 core location at 122 mcd, which may have stemmed from increased phytoplankton growth rates. However, decreased pCO_2 may also have contributed to the ε_p decrease, resulting from widespread marine organic carbon burial at the onset of OAE2 proper (Arthur et al., 1987; Schlanger & Jenkyns, 1976).

Both terrestrial and marine biomarkers in the SH#1 core indicate a short-lived pulse of CO_2 during the middle of the CIE (120.6 mcd; Figures 2–6). A pulse of isotopically light carbon during the CIE phase is also evident in carbon isotope records from terrestrial biomarkers off the coast of northwest Africa (Kuypers et al., 1999), indicating a globally relevant carbon cycle perturbation. While the overall trend of the CIE phase reflects global-scale organic carbon burial (e.g., Owens et al., 2018), the concomitant punctuation of isotopically light carbon in both marine and terrestrial biomarkers likely indeed reflects a pulse of isotopically light CO_2 to the ocean-atmosphere system (Figure 6d). While some studies have shown evidence of forest fires in the western US during the middle of the initial CIE (Baker et al., 2019), other studies of the SH#1 core have not shown such evidence (Boudinot & Sepúlveda, 2020), highlighting uncertainties in the sources and extent of such CO_2 pulse at this interval. The similarities in terrestrial biomarker $\delta^{13}C$ records from the WIS (this study) and the Atlantic basin (Kuypers et al., 1999) with marine biomarkers and resulting pCO_2 estimates (Figure 6d) do support the interpretation of globally increased pCO_2 even during the initial CIE, and ultimately highlights the dynamic nature of the global carbon cycle at the onset of OAE2.

ε_p estimates show two spikes during the Plenus (at the beginning and toward the middle, ~119.5 and ~118 mcd; Figure 6b), punctuated by a decrease at 119 mcd (Figure 6b). Those samples showing elevated ε_p values in the Plenus also show some of the highest concentrations of chloroacetate (Boudinot et al., 2020), a biomarker indicative of euxinic conditions in the photic zone likely driven by increased marine productivity an/or enhanced water column stratification (e.g., Sinninghe Damsté & Schouten, 2006). Thus, the increases in ε_p during the Plenus do not likely reflect decreased productivity, and most likely reflect pulses of increased pCO_2. A number of previous studies have also evidenced increased pCO_2 during the Plenus (e.g., Barclay et al., 2010; Boudinot & Sepúlveda, 2020; O'Connor et al., 2019; van Bentum et al., 2012). The magnitude of the two-phased pCO_2 increase during the Plenus from this record (~200 ppm; Figure 6d) is similar to that of pCO_2 records from both stomatal indices from the western US (Barclay et al., 2010) and carbon isotopes from the Demerara Rise (van Bentum et al., 2012). While the first spike in pCO_2 during the Plenus (~119.5 mcd) does correspond with a bentonite layer ("Bentonite A," Boudinot et al., 2020; Jones et al., 2019; Figure 6), the second (~118 mcd) does not, making lithologic or volcanic explanations of the carbon cycle changes observed during the Plenus in the SH#1 core incomplete. However, magmatic outgassing has been invoked to explain the pulse of ^{13}C-depleted CO_2 during the Plenus (e.g., Barclay et al., 2010; Kuroda & Ohkouchi, 2006), as has sea-floor carbon oxidation (Jenkyns et al., 2017), and forest fires (Boudinot & Sepúlveda, 2020). The stratigraphic correlation of the two-phased increase in forest fires (~119 and ~117 mcd; Boudinot & Sepúlveda, 2020) with the changes in pCO_2 (Figure 6d) provides a potential explanation for the multiple pulses of atmospheric CO_2 during the Plenus, though more work is required to disentangle the relationship between regional evidence of forest fires (Boudinot & Sepúlveda, 2020), sedimentary evidence of local volcanism ("Bentonite A," Boudinot et al., 2020; Elder, 1988; Jones et al., 2019), and global changes in pCO_2. Overall, the SH#1 core pCO_2 record indicates that the Plenus interval experienced dynamic carbon cycle changes, including pulses of CO_2 to the ocean-atmosphere system (e.g., O'Connor et al., 2019), rather than a simple decrease in pCO_2 driven by carbon burial (e.g., Jarvis et al., 2011; Jenkyns et al., 2017; Sinninghe Damste et al., 2010).

After the Plenus, changes in ε_p and pCO_2 are comparably minor, with ε_p estimates increasing only slightly through the plateau phase of OAE2 (Figure 6). Although fewer data are available for the plateau phase compared to the preceding intervals, trends in the SH#1 core suggest that the global carbon cycle was more stable during the plateau than early in the event.

A notable increase in ε_p after the event (~99 mcd; Figure 6b) corresponds with an increase in the concentration of algal steranes and bacterial hopanes (Boudinot et al., 2020), an increase in the relative abundance of the planktic foraminifera Planoheterohelix (Boudinot et al., 2020), the maximum transgressive phase of the Greenhorn Cyclothem (Jones et al., 2019), and bentonite bed D (Figure 6; Jones et al., 2019). These together

indicate an increase in productivity at the SH#1 core location after OAE2, coinciding with another pulse of CO_2 (Figures 6c and 6d) potentially derived from volcanic activity (indicated by bentonite bed D).

4.4.3. Comparison With Other pCO_2 Records

Estimates of pCO_2 during OAE2 from deeper-water environments are generally consistent with those from the SH#1 core, though most show a wider range of pCO_2 (Barclay et al., 2010; Freeman & Hayes, 1992; Sinninghe Damsté et al., 2008; van Bentum et al., 2012). Sulfur-bound phytane-derived pCO_2 estimates from the Cape Verde Basin (eastern equatorial Atlantic; Sinninghe Damsté et al., 2008; *b*-value = 170) suggest 1,300 ppm before OAE2, ~800–1,000 ppm during the CIE, and ~1,300 ppm at the end of OAE2. Sulfur-bound phytane-derived pCO_2 estimates from the Demerara Rise (western equatorial Atlantic; van Bentum et al., 2012; *b*-values from 120 to 220) indicate a range of 1,000–2,300 ppm before OAE2, 700–1,400 ppm during the CIE phase, 700–2,300 during the Plenus, 500–2,000 ppm in the plateau, and 700–2,200 ppm after OAE2. Geoporphyrin carbon isotope-derived pCO_2 estimates from the WIS during the plateau of OAE2 suggest a range of 910–1,100 ppm (Freeman & Hayes, 1992). The general agreement between the pCO_2 estimates from the SH#1 core and other records provides confidence in our use of $\delta^{13}C_{marine\text{-}lipid}$ in the western margin of the WIS as a record of changes in global carbon cycle perturbations. That the record from a marginal location in the WIS is corroborated by other records from deeper locations and other basins highlights the global nature of the carbon cycle perturbations recorded in sedimentary sections during OAE2, and supports previous work demonstrating that variability in ocean basin conditions is compatible with globally correlative carbon cycle impacts (Kuroda & Ohkouchi, 2006; Owens et al., 2018). High-resolution sampling from the SH#1 core also provides new insight into shorter-lived carbon cycle perturbations, including multiple pulses of CO_2 input before and during the OAE2 event, that were not identified in previous, coarser-resolution investigations because these shorter-lived perturbations are consistent in tracers of atmospheric carbon (terrestrial biomarkers) and marine carbon (marine biomarkers) in the SH#1 core, they are likely indicative of global-scale dynamics.

5. Conclusions

We leveraged the expanded organic-rich sedimentary record from a marginal marine setting in the WIS to reconstruct changes in the carbon isotopic composition of inorganic carbon pools, atmospheric pCO_2, and marine productivity using compound-specific carbon isotope analyses of marine-derived and terrestrially derived biomarkers. The resulting records corroborate changes in carbon cycling that are well established (e.g., the globally correlated OAE2 chemostratigraphic phases, general range of atmospheric pCO_2), while also revealing shorter-lived carbon cycle perturbations during the event that have not previously been described (e.g., an input of isotopically light carbon during the CIE phase).

Using the information on carbon isotope fractionation during plant wax biosynthesis, we show that $\delta^{13}C_{plant\text{-}wax}$ can be used to estimate $\delta^{13}C_{CO_2}$. These estimates from the SH#1 core provide new constraints on the carbon cycle during OAE2 that will support future investigations of global carbon cycle dynamics. High-resolution records of $\delta^{13}C_{CO_2}$, $\delta^{13}C_{CO_{2-aq}}$, and pCO_2 all show pulses of CO_2 input before the OAE2 event, during the CIE phase, and during the Plenus interval. The range of pCO_2 estimates from marine biomarkers from the SH#1 core's marginal setting in the WIS is consistent with records from pelagic sections, and from other pCO_2 proxies, supporting the utility of this proxy in marginal marine settings.

While previous studies inferred that OAE2 was a singular, global response to a flux of CO_2 and nutrients before the event, our high-resolution compound-specific carbon isotope study suggests that OAE2 was the culmination of multiple carbon cycle perturbations. Further insights into the ecosystem-scale responses to CO_2 inputs and burial during OAE2 will help to understand the complex carbon cycle and biological dynamics during the event.

Conflict of Interest

The authors declare no conflicts of interest relevant to this study.

Data Availability Statement

Data sets for this study are available at Pangaea (Boudinot et al., 2021). Compound-specific carbon isotope results from the SH#1 core were analyzed and processed at the University of Colorado Boulder. PANGAEA, https://doi.org/10.1594/PANGAEA.933277.

Acknowledgments
The authors thank members of the Organic Geochemistry Lab at the University of Colorado Boulder, including undergraduate assistants J. van Oosten, T. Bond, S. Gandhi-Besbes, J. Straight, S. Tostanoski, A. Mcquade, H. Nguyen, S. Moran, and J. Lopez for laboratory assistance. Additionally, the authors thank B. Davidheiser-Kroll and K. Snell from the CUBES lab at CU Boulder for help with the organic carbon analysis. The authors also thank the members of the Collaborative Research: Perturbation of the Marine Food Web and Extinction during the Oceanic Anoxic Event at the Cenomanian/Turonian, B. Sageman, M. Jones, T. Bralower, R. L. Oakes, M. Leckie, and A. L. Parker for field activities, sample collection, and fruitful discussions. Furthermore, the authors thank A. Titus (BLM, Grand Staircase-Escalante National Monument) for prospecting coring sites and obtaining collecting permits, J. Spencer (U.S. National Park Service Glen Canyon Recreational Area) for accessing outcrop sections, and J. Parlett, S. Crawford, and the western U.S. Geological Survey drilling crew, and C. Lowery, S. Karduck, Q. Li, M. Wnuk, and L. Victoria for sample collection during fieldwork. This study was funded by the NSF Division of Earth Sciences, Earth-Life Transitions (ELT) program through grant #1338318, and by the American Chemical Society Petroleum Research Fund (ACS-PRF)—Doctoral New Investigator Award #58815-DNI2. F. G. Boudinot acknowledges support from the Department of Geological Sciences at the University of Colorado Boulder.

References

Arthur, M. A., Schlanger, S. O., & Jenkyns, H. C. (1987). The Cenomanian-Turonian Oceanic Anoxic Event, II. Palaeoceanographic controls on organic-matter production and preservation. In J. Brooks, & A. J. Fleet (Eds.), *Marine petroleum source rocks* (pp. 401–420). London Geological Society. https://doi.org/10.1144/GSL.SP.1987.026.01.25

Baker, S. J., Belcher, C. M., Barclay, R. S., Hesselbo, S. P., Laurin, J., & Sageman, B. B. (2019). CO_2-induced climate forcing on the fire record during the initiation of Cretaceous Oceanic Anoxic Event 2. *GSA Bulletin*, *132*(1–2), 321–333. https://doi.org/10.1130/B35097.1

Barclay, R. S., McElwain, J. C., & Sageman, B. B. (2010). Carbon sequestration activated by a volcanic CO_2 pulse during Ocean Anoxic Event 2. *Nature Geoscience*, *3*, 205–208. https://doi.org/10.1038/ngeo757

Belcher, C. M., & Hudspith, V. A. (2016). Changes to Cretaceous surface fire behavior influenced the spread of the early angiosperms. *New Phytologist*, *213*(3), 1521–1532. https://doi.org/10.1111/nph.14264

Bice, K. L., Birgenl, D., Meyers, P. A., Dahl, K. A., Hinrichs, K.-U., & Norris, R. D. (2006). A multiple proxy and model study of Cretaceous upper ocean temperatures and atmospheric CO_2 concentrations. *Paleoceanography*, *21*(2), PA2002. https://doi.org/10.1029/2005pa001203

Bohm, F., Joachimski, M. M., Lehnert, H., Morgenroth, G., Kretschmer, W., Vacelet, J., & Fullo, W.-C. (1996). Carbon isotope records from extant Caribbean and South Pacific sponges: Evolution of $\delta^{13}C$ in surface water DIC. *Earth and Planetary Science Letters*, *139*(1–2), 291–303. https://doi.org/10.1016/0012-821X(96)00006-4

Boudinot, F. G., Dildar, N., Leckie, R. M., Parker, A., Jones, M. M., Sageman, B. B., et al. (2020). Neritic ecosystem response to Oceanic Anoxic Event 2 in the Cretaceous Western Interior Seaway, USA. *Palaeogeography, Palaeoclimatology, Palaeoecology*, *546*, 109673. https://doi.org/10.1016/j.palaeo.2020.109673

Boudinot, F. G., Kopf, S., Dildar, N., & Sepúlveda, J. (2021). *Compound-specific carbon isotope results from the SH#1 core analyzed and processed at University of Colorado Boulder*. PANGAEA. https://doi.org/10.1594/PANGAEA.933277

Boudinot, F. G., & Sepúlveda, J. (2020). Forest fires in response to marine carbon burial: Evidence from the Cretaceous Oceanic Anoxic Event 2. *Nature Geoscience*, *13*, 693–698. https://doi.org/10.1038/s41561-020-0633-y

Boudinot, F. G., & Wilson, J. (2020). Does a proxy measure up? A framework to assess and convey proxy reliability. *Climate of the Past*, *16*, 1807–1820. https://doi.org/10.5194/cp-16-1807-2020

Bralower, T. J. (1988). Calcareous nannofossil biostratigraphy and assemblages of the Cenomanian-Turonian boundary interval: Implications for the origin and timing of oceanic anoxia. *Paleoceanography*, *3*(3), 275–316. https://doi.org/10.1029/pa003i003p00275

Bridigare, R. R., Fluegge, A., Fremman, K. H., Hanson, K. L., Hayes, J. M., Hollander, D., et al. (1997). Consistent fractionation of ^{13}C in nature and in the laboratory: Growth-rate effects in some haptophyte algae. *Global Biogeochemical Cycles*, *11*(2), 279–292. https://doi.org/10.1029/96GB03939

Brodie, C. R., Leng, M. J., Casford, J. S. L., Kendrick, C. P., Lloyd, J. M., Yongqiang, Z., & Bird, M. I. (2011). Evidence for bias in C and N concentrations and $\delta^{13}C$ composition of terrestrial and aquatic organic materials due to pre-analysis acid preparation methods. *Chemical Geology*, *282*(3–4), 67–83. https://doi.org/10.1016/j.chemgeo.2011.01.007

Deuser, W. G., & Degens, E. T. (1976). Carbon isotope fractionation in the system CO_2 (gas)-CO_2(aqueous)-HCO_3(aqueous). *Nature*, *215*, 1033–1035. https://doi.org/10.1038/2151033a0

Diefendorf, A. F., Freeman, K. H., Wing, S. L., & Graham, H. V. (2011). Production of n-alkyl lipids in living plants and implications for the geologic past. *Geochimica et Cosmochimica Acta*, *75*(23), 7472–7485. https://doi.org/10.1016/j.gca.2011.09.028

DuVivier, A. D. C., Selby, D., Sageman, B. B., Jarvis, I., Grocke, D. R., & Voigt, S. (2014). Marine $^{187}Os/^{188}Os$ isotope stratigraphy reveals the interaction of volcanism and ocean circulation during Oceanic Anoxic Event 2. *Earth and Planetary Science Letters*, *389*, 23–33. https://doi.org/10.1016/j.epsl.2013.12.024

Eglinton, G., & Hamilton, R. J. (1967). Leaf epicuticular waxes. *Science*, *156*(3780), 1322–1335. https://doi.org/10.1126/science.156.3780.1322

Ehleringer, J. R., & Cerling, T. E. (2001). Photosynthetic pathways and climate. In E.-D. Schulze, M. Heimann, S. Harrison, E. Holland, J. Lloyd, I. C. Prentice, & D. Schimel (Eds.), *Global biogeochemical cycles in the climate system* (pp. 267–277). Academic. https://doi.org/10.1016/b978-012631260-7/50023-6

Eicher, D. L., & Diner, R. (1985). Foraminifera as indicators of water mass in the Cretaceous Greenhorn Sea, western interior. In L. M. Pratt, E. G. Kauffman, & F. B. Zelt (Eds.), *Fine-grained deposits and biofacies of the Cretaceous Western Interior Seaway: Evidence of cyclic sedimentary processes. Society of economic paleontologists and mineralogists field trip guidebook* (Vol. 4, pp. 60–71). Society of Economic Paleontologists and Mineralogists.

Elder, W. P. (1988). Geometry of upper Cretaceous benotinite beds: Implictions about volcanic source areas of paleowind patterns, western interior, United States. *Geology*, *16*, 835–838. https://doi.org/10.1130/0091-7613(1988)016<0835:GOUCBB>2.3.CO;2

Elderbak, K., & Leckie, R. M. (2016). Paleocirculation and foraminiferal assemblages of the Cenomanian-Turonian Bridge Creek Limestone bedding couplets: Productivity vs. dilution during OAE2. *Cretaceous Research*, *60*, 52–77. https://doi.org/10.1016/j.cretres.2015.11.009

Erbacher, J., Friedrich, O., Wilson, P. A., Birch, H., & Mutterlose, J. (2005). Stable organic carbon isotope stratigraphy across Oceanic Anoxic Event 2 of Demerara Rise, western tropical Atlantic. *Geochemistry, Geophysics, Geosystems*, *6*(6), 1–9. https://doi.org/10.1029/2004GC000850

Freeman, K. H., & Hayes, J. M. (1992). Fractionation of carbon isotopes by phytoplankton and estimates of ancient CO_2 levels. *Global Biogeochemical Cycles*, *6*(2), 185–198. https://doi.org/10.1029/92GB00190

Gale, A. S., & Christensen, W. K. (1996). Occurrence of the belemnite Actinocamax plenus in the Cenomanian of SE France and its significance. *Bulletin of the Geological Society of Denmark*, *43*, 68–77. https://doi.org/10.37570/bgsd-1996-43-08

Goericke, R., & Fry, B. (1994). Variations of marine plankton $\delta^{13}C$ with latitude, temperature, and dissolved CO_2 in the world ocean. *Global Biogeochemical Cycles*, *8*(1), 85–90. https://doi.org/10.1029/93GB03272

Grocke, D. R. (2002). The carbon isotope composition of ancient CO_2 based on higher-plant organic matter. *Philosophical Transations of the Royal Society of London A*, *360*(1793), 633–658. https://doi.org/10.1098/rsta.2001.0965

Gruber, N., Keeling, C. D., Bacastow, R. B., Guenther, P. R., Lueker, T. J., Wahlen, M., et al. (1999). Spatiotemporal patterns of carbon-13 in the global surface oceans and the oceanic Suess effect. *Global Biogeochemical Cycles*, *13*(2), 307–335. https://doi.org/10.1029/1999GB900019

Hay, W. W., Wold, C. N., & DeConto, R. M. (1996). The role of salinity in circulation of the Cretaceous ocean. *Zentralblatt für Geologie und Paläontologie, Teil I*, *1996*, 1445–1454.

Hayes, J. M. (2001). Fractionation of the isotopes of carbon and hydrogen in biosynthetic processes. *Reviews in Mineralogy and Geochemistry*, *43*, 225–277. https://doi.org/10.2138/gsrmg.43.1.225

Hayes, J. M., Freeman, K. H., Popp, B. N., & Hoham, C. H. (1990). Compound-specific isotope analyses: A novel tool for reconstruction of ancient biogeochemical processes. *Organic Geochemistry*, *16*(4–6), 1115–1128. https://doi.org/10.1016/0146-6380(90)90147-R

Hernández-Almeida, I., Krumhardt, K. M., Zhang, H., & Stoll, H. M. (2020). Estimation of physiological factors controlling carbon isotope fractionation in coccolithophores in photic zone and core-top samples. *Geochemistry, Geophysics, Geosystems*, *21*(11), e2020GC009272. https://doi.org/10.1029/2020GC009272

Hilbrecht, H., & Hoefs, J. (1986). Geochemical and palaeontological studies of the $\delta^{13}C$ anomaly in boreal and north Tethyan Cenomanian-Turonian sediments in Germany and adjacent areas. *Palaeogeogrpahy, Palaeoclimatology, Palaeoecology*, *53*(2–4), 169–189. https://doi.org/10.1016/0031-0182(86)90043-X

Hollis, C. J., Jones, T. D., Anagnostou, E., Bijl, P. K., Cramwinckel, M. J., Cui, Y., et al. (2019). The DeepMIP contribution to PMIP4: Methodologies for selection, compilation and analysis of latest Paleocene and early Eocene climate proxy data, incorporating version 0.1 of the DeepMIP database. *Geoscientific Model Development*, *12*, 3149–3206. https://doi.org/10.5194/gmd-12-3149-2019

Hong, S. K., & Lee, Y. I. (2012). Evaluation of atmospheric carbon dioxide concentrations during the Cretaceous. *Earth and Planetary Science Letters*, *327–328*, 23–28. https://doi.org/10.1016/j.epsl.2012.01.014

Huber, B. T., Norris, R. D., & MacLeod, K. G. (2002). Deep-sea paleotemperature record of extreme warmth during the Cretaceous. *Geology*, *30*(2), 123–136. https://doi.org/10.1130/0091-7613(2002)030<0123:DSPROE>2.0.CO;2

Humphreys, M. P., Achterberg, E. P., Griffith, AM., McDonald, A., & Boyce, A. J. (2015). Measurement of the stable carbon isotope composition of dissolved inorganic carbon in the northeastern Atlantic and Nordic Seas during summer 2012. *Earth Systems Science Data*, *7*, 127–135. https://doi.org/10.5194/essd-7-127-2015

Jarvis, I., Lignum, J. S., Grocke, D. R., Jenkyns, H. C., & Pearce, M. A. (2011). Black shale deposition, atmospheric CO_2 drawdown, and cooling during the Cenomanian-Turonian Oceanic Anoxic Event. *Paleoceanography*, *26*(3), PA3201. https://doi.org/10.1029/2010PA002081

Jenkyns, H. C., Dickson, A. J., Ruhl, M., & van den Boorn, S. H. J. M. (2017). Basalt-seawater interaction, the Plenus Cold Event, enhanced weathering and geochemical change: Deconstructing Oceanic Anoxic Event 2 (Cenomanian-Turonian, Late Cretaceous). *Sedimentology*, *64*, 16–43. https://doi.org/10.1111/sed.12305

Jones, M. M., Sageman, B. B., Oakes, R. L., Parker, A. L., Leckie, R. M., Bralower, T. J., et al. (2019). Astronomical pacing of relative sea level during Oceanic Anoxic Event 2: Preliminary studies of the expanded SH#1 core, Utah. *GSA Bulletin*, *131*(9–10), 1702–1722. https://doi.org/10.1130/B32057.1

Jones, M. M., Sageman, B. B., Selby, D., Jicha, B. R., Singer, B. S., & Titus, A. L. (2020). Regional chronostratigraphic synthesis of the Cenomanian-Turonian Oceanic Anoxic Event 2 (OAE2) interval, Western Interior Basin (USA): New Re-Os chemostratigraphy and 40Ar/39Ar geochronology. *Geological Society of America Bulletin*, *133*, 1090–1104. https://doi.org/10.1130/B35594.1

Kauffman, E. G. (1984). Paleobiogeography and evolutionary response dynamic in the Cretaceous Western Interior Seaway of North America. In G. E. G. Westermann (Ed.), *Jurassic-Cretaceous biochronology and paleogeography of North America* (pp. 273–306). Geological Association of Canada.

Kuroda, J., & Ohkouchi, N. (2006). Implications of spatiotemporal distribution of black shales deposited during the Cretaceous Oceanic Anoxic Event-2. *Paleontological Research*, *10*(4), 345–358. https://doi.org/10.2517/prpsj.10.345

Kuypers, M. M. M., Pancost, R. D., Nijenhuis, I. A., & Sinninghe Damsté, J. S. (2002). Enhanced productivity led to increased organic carbon burial in the euxinic North Atlantic basin during the late Cenomanian oceanic anoxic event. *Paleoceanography*, *17*, 1051. https://doi.org/10.1029/2000PA000569

Kuypers, M. M. M., Pancost, R. D., & Sinninghe Damsté, J. S. (1999). A large and abrupt fall in atmospheric CO_2 concentration during Cretaceous times. *Nature*, *399*, 342–345. https://doi.org/10.1038/20659

Leckie, R. M. (1985). Foraminifera of the Cenomanian-Turonian Boundary interval, Greenhorn Formation, Rock Canyon Anticline, Pueblo, Colorado. In L. M. Prattt, E. G. Kauffman, & F. B. Zelt (Eds.), *Fine-grained deposits and biofacies of the Cretaceous Western Interior Seaway: Evidence of cyclic sedimentary processes* (pp. 139–149). Society of Economic Paleontologists and Mineralogists.

Leckie, R. M., Bralower, T. J., & Cashman, R. (2002). Oceanic anoxic event and plankton evolution: Biotic response to tectonic forcing during the mid-Cretaceous. *Paleoceanography*, *17*, PA000623. https://doi.org/10.1029/2001PA000623

Minoletti, F., de Rafelis, M., Renard, M., Gardin, S., & Young, J. (2005). Changes in the pelagic fine fraction carbonate sedimentation during the Cretaceous-Paleocene transition: Contribution of the separation technique to the study of Bidart section. *Palaeogeography*, *216*(1–2), 119–137. https://doi.org/10.1016/j.palaeo.2004.10.006

Monteiro, F. M., Pancost, R. D., Ridgwell, A., & Donnadieu, Y. (2012). Nutrients as the dominant control on the spread of anoxia and euxinia across the Cenomanian-Turonian oceanic anoxic event (OAE2): Model-data comparison. *Paleoceanography*, *27*, 1–17. https://doi.org/10.1029/2012PA002351

Mook, W. G., Bommerson, J. C., & Staverman, W. H. (1974). Carbon isotope fractionation between dissolved bicarbonate and gaseous carbon dioxide. *Earth and Planetary Science Letters*, *22*(2), 169–176. https://doi.org/10.1016/0012-821X(74)90078-8

Mort, H. P., Adatte, T., Follmi, K. B., Keller, G., Steinmann, P., Matera, V., et al. (2007). Phosphorus and the roles of productivity and nutrient recycling during Oceanic Anoxic Event 2. *Geology*, *35*(6), 483–486. https://doi.org/10.1130/G23475A.1

O'Brien, C. L., Robinson, S. A., Pancost, R. D., Sinninghe Damsté, J. S., Schouten, S., Lunt, D. J., et al. (2017). Cretaceous sea-surface temperature evolution: Concentrations from TEX_{86} and planktonic foraminiferal oxygen isotopes. *Earth-Science Reviews*, *172*, 224–247. https://doi.org/10.1016/j.earscirev.2017.07.012

O'Connor, L. K., Jenkyns, H. C., Robinson, S. A., Remmelzwaal, S. R. C., Batenburg, S. J., Parkinson, I. J., & Gale, A. S. (2019). A re-evaluation of the Plenus Cold Event, and the links between CO_2, temperature, and seawater chemistry during OAE2. *Paleoceanography and Paleoclimatology*, *35*(4), e2019PA003631. https://doi.org/10.1029/2019PA003631

Ohkouchi, N., Ogawa, N. O., Chikaraishi, Y., Tanaka, H., & Wada, E. (2015). Biochemical and physiological bases for the use of carbon and nitrogen isotopes in environmental and ecological studies. *Progress in Earth and Planetary Science*, *2*, 1–17. https://doi.org/10.1186/s40645-015-0032-y

Osbourne, C. P., & Beerling, D. J. (2006). Nature's green revolution: The remarkable evolution rise of C_4 plants. *Philosophical Transactions of the Royal Society B*, *361*(1465), 173–194. https://doi.org/10.1098/rstb.2005.1737

Ostrander, C. M., Owens, J. D., & Nielsen, S. G. (2017). Constraining the rate of oceanic deoxygenation leading up to a Cetaceous Oceanic Anoxic Event (OAE-2: ~94 Ma). *Science Advances*, *3*(8), e1701020. https://doi.org/10.1126/sciadv.1701020

Owens, J. D., Gill, B. C., Jenkyns, H. C., Bates, S. M., Sevemnn, S., Kuypers, M. M., et al. (2013). Sulfur isotopes track the global extent and dynamics of euxinia during Cretaceous Oceanic Anoxic Event 2. *Proceedings of the National Academy of Science of the United States of America*, *110*(46), 18407–18412. https://doi.org/10.1073/pnas.1305304110

Owens, J. D., Lyons, T. W., & Lowery, C. M. (2018). Quantifying the missing sink for global organic carbon burial during a Cretaceous oceanic anoxic event. *Earth and Planetary Science Letters*, *499*, 83–94. https://doi.org/10.1016/j.epsl.2018.07.021

Owens, J. D., Reinhard, C. T., Rohrssen, M., Love, G. D., & Lyons, T. W. (2016). Empirical links between trace metal cycling and marine microbial ecology during a large perturbation to Earth's carbon cycle. *Earth and Planetary Science Letters*, *449*, 407–417. https://doi.org/10.1016/j.epsl.2016.05.046

Pagani, M. (2014). Biomarker-based inferences of past climate: The alkenone pCO_2 proxy. In H. D. Holland, & K. K. Turekian (Eds.), *Treatise on geochemistry* (2nd ed., Vol. 12, pp. 361–378). Springer. https://doi.org/10.1016/B978-0-08-095975-7.01027-5

Pagani, M., Freeman, K. H., Ohkouchi, N., & Caldeira, K. (2002). Comparison of water column [CO_{2aq}] with sedimentary alkenone-based estimates: A test of the alkenone-CO_2 proxy. *Paleoceanography*, *17*(4), 1069. https://doi.org/10.1029/2002PA000756

Pancost, R. D., Crawford, N., Magness, S., Turner, A., Jenkyns, H. C., & Maxwell, J. R. (2004). Further evidence for the development of photic-zone euxinic conditions during Mesozoic oceanic anoxic events. *Journal of the Geological Society, London*, *161*, 353–364. https://doi.org/10.1144/0016764903-059

Pancost, R. D., Freeman, K. H., & Arthur, M. A. (1998). Organic geochemistry of the Cretaceous Western Interior Seaway: A trans-basinal evaluation. In W. Dean, & M. A. Arthur (Eds.), *Stratigraphy and paleoenvironments of the Cretaceous Western Interior Seaway, USA. SEPM concepts in sedimentology and paleontology* (pp. 173–188). Society of Economic Paleontologists and Mineralogists. https://doi.org/10.2110/csp.98.06.0173

Pancost, R. D., Freeman, K. H., Wakeham, S. G., & Robertson, C. Y. (1997). Controls on the carbon isotope fraction by diatoms in the Peru upwelling region. *Geochimica et Cosmochimica Acta*, *61*(23), 4983–4991. https://doi.org/10.1016/S0016-7037(97)00351-7

Petersen, S. V., Tabor, C. R., Lohmann, K. C., Poulsen, C. J., Meyer, K. W., Carpenter, S. J., et al. (2016). Temperature and salinity of the Late Cretaceous Western Interior Seaway. *Geology*, *44*(11), 903–906. https://doi.org/10.1130/G38311.1

Popp, B. N., Takigiku, R., Hayes, J. M., Louda, J. W., & Baker, E. W. (1989). The post-Paleozoic chronology and mechanism of ^{13}C depletion in primary marine organic matter. *American Journal of Science*, *289*(4), 436–454. https://doi.org/10.2475/ajs.289.4.436

R Core Team. (2017). *R: A language and environment for statistical computing*. R Foundation for Statistical Computing. Retrieved from https://www.R-project.org/

Reolid, M., Sanchez-Quinonez, C. A., Alegret, L., & Molina, E. (2015). Palaeoenvironmental turnover across the Cenomanian-Turonian transition in Oued Bahloul, Tunisia: Foraminifera and geochemical proxies. *Palaeogeography, Palaeoclimatology, Palaeoecology*, *417*, 491–510. https://doi.org/10.1016/j.palaeo.2014.10.011

Riebesell, U., Revill, A. T., Holdsworth, D. G., & Volkman, J. K. (2002). The effects of varying CO_2 concentration on lipid composition and carbon isotope fractionation in *Emiliania huxleyi*. *Geochmiica et Cosmochimica Acta*, *64*(24), 4179–4192. https://doi.org/10.1016/S0016-7037(00)00474-9

Romanek, C. S., Grossman, E. L., & Morse, J. W. (1992). Carbon isotopic fractionation in synthetic aragonite and calcite: Effects of temperature and precipitation rate. *Geochimica et Cosmochimica Acta*, *56*(1), 419–430. https://doi.org/10.1016/0016-7037(92)90142-6

Sage, R. F. (2004). The evolution of C_4 photosynthesis. *New Phytologist*, *161*(2), 341–370. https://doi.org/10.1111/j.1469-8137.2004.00974.x

Sageman, B. B., & Arthur, M. A. (1994). Early Turonian paleogeographic/paleobathymetric map, Western Interior, U.S. In M. V. Caputo, J. A. Peterson, & K. J. Franczyk (Eds.), *Mesozoic systems of the Rocky Mountain Region, U.S, Special Publication* (pp. 457–470). Rocky Mountain Section—Society of Economic Paleontologists and Mineralogists.

Sageman, B. B., Meyers, S. R., & Arthur, M. A. (2006). Orbital time scale and new C-isotope record for Cenomanian-Turonian boundary stratotype. *Geology*, *34*(2), 125–128. https://doi.org/10.1130/G22074.1

Sakata, S., Hayes, J. M., McTaggert, A. R., Evans, R. A., Leckrone, K. J., & Togasaki, R. K. (1997). Carbon isotopic fractionation associated with lipid biosynthesis by a cyanobacterium: Relevance for interpretation of biomarker records. *Geochimica et Cosochimica Acta*, *61*(24), 5379–5389. https://doi.org/10.1016/S0016-7037(97)00314-1

Sarmiento, J. L., Herbert, T. D., & Toggweiler, J. R. (1988). Causes of anoxia in the world ocean. *Global Biogeochemical Cycles*, *2*(2), 115–128. https://doi.org/10.1029/GB002i002p00115

Schlanger, S. O., Arthur, M. A., Jenkyns, H. C., & Scholle, P. A. (1987). The Cenomanian-Turonian Oceanic Anoxic Event, I. Stratigraphy and distribution of organic carbon-rich beds and the marine $\delta^{13}C$ excursion. In J. Brooks, & A. J. Fleet (Eds.), *Marine petroleum source rocks* (pp. 371–399). Geological Society. https://doi.org/10.1144/GSL.SP.1987.026.01.24

Schlanger, S. O., & Jenkyns, H. C. (1976). Cretaceous oceanic anoxic events: Causes and consequences. *Geologie en Mijnbouw*, *55*, 179–184.

Scholle, P. A., & Arthur, M. A. (1980). Carbon isotope fluctuations in Cretaceous pelagic limestones: Potential stratigraphic and petroleum exploration tool. *The American Association of Petroleum Geologists Bulletin*, *64*(1), 67–87. https://doi.org/10.1306/2F91892D-16CE-11D7-8645000102C1865D

Schouten, S., Klein Bretelier, W. C. N., Blokker, P., Shogt, N., Rijpstra, W. I. C., Grice, K., et al. (1998). Biosynthetic effects on the stable carbon isotopic compositions of algal lipids: Implications for deciphering the carbon isotopic biomarker record. *Geochimica et Cosmochimica Acta*, *62*(8), 1397–1406. https://doi.org/10.1016/S0016-7037(98)00076-3

Scotese, C. (2014). Atlas of Late Cretaceous paleogeographic maps, PALEOMAP Atlas for ArcGIS, volume 2, The Cretaceous, Maps 16-22, Mollweide Projection, PALEOMAP Project.

Sepúlveda, J., Alegret, L., Thomas, E., Haddad, E., Cao, C., & Summons, R. E. (2019). Stable isotope constraints on marine productivity across the Cretaceous-Paleogene mass extinction. *Paleoceanography and Paleoclimatology*, *34*(7), 1195–1217. https://doi.org/10.1029/2018PA003442

Sepúlveda, J., Wendler, J., Leider, A., Kuss, H. J., Summons, R. E., & Hinrichs, K. U. (2009). Molecular isotopic evidence of environmental and ecological changes across the Cenomanian-Turonian boundary in the Levant Platform of Central Jordan. *Organic Geochemistry*, *40*, 553–568. https://doi.org/10.1016/j.orggeochem.2009.02.009

Sheu, D. D., LeeWang, W. Y., Wei, C. L., Chen, C. T. A., Cherng, C., Huang, M. H., & Huang, M. H. (1996). Depth distribution of $\delta^{13}C$ of dissolved ΣCO_2 in seawater off eastern Taiwan: Effects of the Kuroshio current and its associated upwelling phenomenon. *Continental Shelf Research*, *16*(12), 1609–1619. https://doi.org/10.1016/0278-4343(95)00085-2

Sinninghe Damsté, J. S., Kuypers, M. M. M., Pancost, R. D., & Schouten, S. (2008). The carbon isotopic response of algae, (cyano)bacteria, archaea and higher plants to the late Cenomanian perturbation of the global carbon cycle: Insights from biomarkers in black shales from the Cape Verde Basin (DSDP Site 367). *Organic Geochemistry*, *39*(12), 1703–1718. https://doi.org/10.1016/j.orggeochem.2008.01.012

Sinninghe Damsté, J. S., & Schouten, S. (2006). Biological markers for anoxia in the photic zone of the water column. In J. K. Volkman (Ed.), *Marine organic matter: Biomarkers, isotopes, and DNA. The Handbook of Environmental Chemistry* (Vol. 2N, pp. 127–163). Springer. https://doi.org/10.1007/698_2_005

Sinninghe Damsté, J. S., van Bentum, E. C., Reichart, G.-J., Pross, J., & Schouten, S. (2010). A CO_2 decrease-driven cooling and increased latitudinal temperature gradient during the mid-Cretaceous Oceanic Anoxic Event 2. *Earth and Planetary Science Letters*, *293*(1–2), 97–103. https://doi.org/10.1016/j.epsl.2010.02.027

Takashima, R., Nishi, H., Huber, B., & Leckie, M. (2006). Greenhouse world and the Mesozoic ocean. *Oceanography*, *19*(4), 82–92. https://doi.org/10.5670/oceanog.2006.07

Tsikos, H., Jenkyns, H. C., Walsworth-bell, B., Petrizzo, M. R., Forster, A., Kolonic, S., et al. (2004). Carbon-isotope stratigraphy recorded by the Cenomanian-Turonian Oceanic Anoxic Event: Correlation and implications based on three key localities. *Journal of the Geological Society, London*. *161*(4), 711–719. https://doi.org/10.1144/0016-764903-077

Turgeon, S. C., & Creasser, R. A. (2008). Cretaceous Oceanic Anoxic Event 2 triggered by a massive magmatic episode. *Nature*, *454*, 323–326. https://doi.org/10.1038/nature07076

van Bentum, E. C., Reichart, G.-J., Forster, A., & Sinninghe Damsté, J. S. (2012). Latitudinal differences in the amplitude of the OAE-2 carbon isotopic excursion: PCO_2 and paleo productivity. *Biogeosciences*, *9*, 717–731. https://doi.org/10.5194/bg-9-717-2012

Weiss, R. F. (1974). Carbon dioxide in water and seawater: The solubility of a non-ideal gas. *Marine Chemistry*, *2*(3), 203–215. https://doi.org/10.1016/0304-4203(74)90015-2

Wilkes, E. B., & Pearson, A. (2019). A general model for carbon isotopes in red-lineage phytoplankton: Interplay between unidirectional processes and fractionation by RubisCO. *Geochimica et Cosmochimica Acta*, *265*, 163–181. https://doi.org/10.1016/j.gca.2019.08.043

Wilson, P., & Norris, R. D. (2001). Warm tropical ocean surface and global anoxia during the mid-Cretaceous period. *Nature*, *412*, 425–429. https://doi.org/10.1038/35086553

Witkowski, C. R., Weijers, J. W. H., Blais, B., Schouten, S., & Sinninghe Damsté, J. S. (2018). Molecular fossils from phytoplankton reveal secular pCO_2 trend over the Phanerozoic. *Science Advances*, *4*(11), eaat4556. https://doi.org/10.1126/sciadv.aat4556

Zhang, Y. G., Pearson, A., Benthien, A., Dong, L., Huybers, P., Liu, X., & Pagani, M. (2019). Refining the alkenone-pCO_2 method I: Lessons from the Quaternary glacial cycles. *Geochimica et Cosmochimica Acta*, *260*, 177–191. https://doi.org/10.1016/j.gca.2019.06.032

References From the Supporting Information

Bonafini, M., Pellegrini, M., Ditchfield, P., & Pollard, A. M. (2013). Investigation of the "canopy effect" in the isotope ecology of temperate woodlands. *Journal of Archaeological Science*, *40*(11), 3926–3935. https://doi.org/10.1016/j.jas.2013.03.028

Collister, J. W., Rieley, G., Stern, B., Eglinton, G., & Fry, B. (1994). Compound-specific $\delta^{13}C$ analysis of leaf lipids from plants with differing carbon dioxide metabolisms. *Organic Geochemistry*, *21*, 619–627. https://doi.org/10.1016/0146-6380(94)90008-6

Diefendorf, A. F., & Freimuth, E. J. (2017). Extracting the most from terrestrial plant-derived n-alkyl lipids and their carbon isotopes from the sedimentary record: A review. *Organic Geochemistry*, *103*, 1–21. https://doi.org/10.1016/j.orggeochem.2016.10.016

Diefendorf, A. F., Leslie, A. B., & Wing, S. L. (2015). Leaf wax composition and carbon isotopes vary among major conifer groups. *Geochimica et Cosmochimica Acta*, *170*, 145–156. https://doi.org/10.1016/j.gca.2015.08.018

Gelpie, E., Schneider, H., Mann, J., & Oru, J. (1970). Hydrocarbons of geochemical significance in microscopic algae. *Phytochemistry*, *9*, 603–612. https://doi.org/10.1016/S0031-9422(00)85700-3

Hayes, J. M. (1993). Factors controlling ^{13}C contents of sedimentary organic compounds: Principles and evidence. *Marine Geology*, *113*, 111–125. https://doi.org/10.1016/0025-3227(93)90153-M

Heimhoffer, U., Hochuli, P. A., Herrle, J. O., Andersen, N., & Weissert, H. (2004). Absence of major vegetation and palaeoatmospheric pCO_2 changes associated with Oceanic Anoxic Event 1a (Early Aptian, SE France). *Earth and Planetary Science Letters*, *223*, 303–318. https://doi.org/10.1016/j.epsl.2004.04.037

Lichtfouse, E., Elbisser, B., Balesdent, J., Mariotti, A., & Bardoux, G. (1994). Isotope and molecular evidence for direct input of maize leaf wax n-alkanes into crop soils. *Organic Geochemistry*, *22*, 349–351. https://doi.org/10.1016/0146-6380(94)90181-3

Lyons, S. L., Baczynski, A. A., Babila, T. L., Bralower, T. J., Hajek, E. A., Kump, L. R., et al. (2019). Palaeocee-Eocene Thermal Maximum prolonged by fossil carbon oxidation. *Nature Geoscience*, *12*, 54–60. https://doi.org/10.1038/s41561-018-0277-3

Magill, C. R., Ashley, G. M., & Freeman, K. H. (2013). Ecosystem variability and early human habitats in eastern Africa. *Proceedings of the National Academy of Science of the United States of America*, *110*, 1167–1174. https://doi.org/10.1073/pnas.1206276110

Riebesell, U., Revill, A. T., Holdsworth, D. G., & Volkman, J. K. (2000). The effects of varying CO_2 concentration on lipid composition and carbon isotope fractionation in *Emiliania huxleyi*. *Geochmiica et Cosmochimica Acta*, *64*, 4179–4192. https://doi.org/10.1016/S0016-7037(00)00474-9

Schubert, B. A., & Jahren, A. H. (2012). The effect of atmospheric CO_2 concentration on carbon isotope fractionation in C_3 land plants. *Geochimica et Cosmochimica Acta*, *96*, 29–43. https://doi.org/10.1016/j.gca.2012.08.003

Sepúlveda, J., Wendler, J., Leider, A., Kuss, H. J., Summons, R. E., & Hinrichs, K. U. (2009). Molecular isotopic evidence of environmental and ecological changes across the Cenomanian-Turonian boundary in the Levant Platform of Central Jordan. *Organic Geochemistry*, *40*, 553–568. https://doi.org/10.1016/j.orggeochem.2009.02.009

Sepúlveda, J., Wendler, J. E., Summons, R. E., & Hinrichs, K.-U. (2009). Rapid resurgence of marine productivity after the Cretaceous-Paleogene mass extinction. *Science*, *326*, 130–132. https://doi.org/10.1126/science.1176233

Talbot, H. M., & Farrimond, P. (2007). Bacterial populations recorded in diverse sedimentary biohopanoid distributions. *Organic Geochemistry*, *38*, 1212–1225. https://doi.org/10.1016/j.orggeochem.2007.04.006

Tissot, B. P., & Welte, D. H. (1984). *Petroleum formation and occurrence* (2nd ed., p. 666). Springer-Verlag.

Volkman, J. K. (2003). Sterols in microorganisms. *Applied Microbiology and Biotechnology*, *60*, 495–506. https://doi.org/10.1007/s00253-002-1172-8

Volkman, J. K., Barrett, S. M., Blackburn, S. I., Mansour, M. P., Sikes, E. L., & Gelin, F. (1998). Microalgal biomarkers: A review of recent research developments. *Organic Geochemistry*, *29*, 1163–1179. https://doi.org/10.1016/S0146-6380(98)00062-X

Wang, Y., & Budd, D. A. (2016). Self-organized pattern formation in sedimentary geochemical systems. In D. A. Budd, E. A. Hajek, & S. J. Purkis (Eds.), *Autogenic dynamics and self-organization in sedimentary systems* (Vol. 106, pp. 67–82), SEPM. https://doi.org/10.2110/sepmsp.106.09